REPORT DOCUMENTATION PAGE

Form Approved
OMB No. 0704-0188

1. AGENCY USE ONLY *(Leave blank)*	2. REPORT DATE 10 Jul 97	3. REPORT TYPE AND DATES COVERED

4. TITLE AND SUBTITLE
SURFACE LAYER FORCED MARINE ATMOSHERIC BOUNDARY LAYER CONVECTIVE EDDIES

5. FUNDING NUMBERS

6. AUTHOR(S)
DAVID JOHN BEBERWYK

7. PERFORMING ORGANIZATION NAME(S) AND ADDRESS(ES)
PENNSYLVANIA STATE UNIVERSITY THE GRADUATE SCHOOL
DEPARTMENT OF METEROLOGY

8. PERFORMING ORGANIZATION REPORT NUMBER
97-083

9. SPONSORING/MONITORING AGENCY NAME(S) AND ADDRESS(ES)
DEPARTMENT OF THE AIR FORCE
AFIT/CI
2950 P STREET
WRIGHT-PATTERSON AFB OH 45433-7765

10. SPONSORING/MONITORING AGENCY REPORT NUMBER

11. SUPPLEMENTARY NOTES

12a. DISTRIBUTION AVAILABILITY STATEMENT

12b. DISTRIBUTION CODE

13. ABSTRACT *(Maximum 200 words)*

DTIC QUALITY INSPECTED 2

14. SUBJECT TERMS

15. NUMBER OF PAGES
76

16. PRICE CODE

17. SECURITY CLASSIFICATION OF REPORT	18. SECURITY CLASSIFICATION OF THIS PAGE	19. SECURITY CLASSIFICATION OF ABSTRACT	20. LIMITATION OF ABSTRACT

The Pennsylvania State University

The Graduate School

Department of Meteorology

SURFACE LAYER FORCED MARINE ATMOSPHERIC

BOUNDARY LAYER CONVECTIVE EDDIES
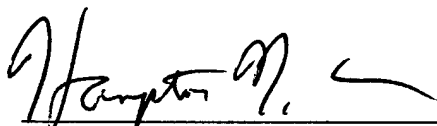
A Thesis in

Meteorology

by

David John Beberwyk

Submitted in Partial Fulfillment
of the Requirements
for the Degree of

Master of Science

August 1997

We approve the thesis of David John Beberwyk.

Date of Signature

_____

Hampton N. Shirer
Associate Professor of Meteorology
Thesis Adviser

6/26/97

_____

Robert Wells
Professor of Mathematics

6/26/97

_____

Dennis W. Thomson
Professor of Meteorology
Head of the Department of Meteorology

26.6.97

ABSTRACT

Boundary layer convective eddies (BLCE) observed via synthetic aperture radar (SAR) on 17 June 1993 during the Hi-Res 2 field experiment are investigated using a three-dimensional nonlinear spectral model derived from the shallow Boussinesq equations. Boundary conditions are appropriate for marine atmospheric boundary layer (MABL) flow and allow for heat and momentum fluxes across the lower boundary, as is required to determine sea-surface stress patterns. Enhancements made to the model for this study include the addition of an inversion layer, an unstable surface layer and weighted nonlinear numerical dissipation. A more numerically accurate integration scheme is also incorporated.

A linear stability analysis of Hi-Res 2 data finds maximum growth rates for disturbances having horizontal wavelengths that match those determined from the 17 June 1993 SAR image. Desirable by-products of the analysis include the determination of physically plausible mean horizontal wind profiles and inversion strengths.

Two model integrations are performed using identical measured atmospheric input values and initial conditions, but with different dissipation weights. The run with weaker dissipation, Case 1, exhibits a fully three-dimensional cellular structure that is consistent with SAR imagery and that is aligned nearly normal to the direction of the mean wind. Case 2, with stronger dissipation, is quasi-two-dimensional and aligned 14^0 to the right of the direction of the mean wind. Cross sections of potential temperature, streamfunction and vertical velocity for both cases reveal that the inversion is capping the BLCE with only minor anomalies in the inversion layer. Magnitudes of several dimensional quantities are compared with observations and/or other studies with encouraging results.

TABLE OF CONTENTS

LIST OF FIGURES

LIST OF TABLES

ACKNOWLEDGMENTS

First and foremost, I am inexpressibly grateful to God, the Father of us all, for giving me the Breath of Life and the fortitude to persevere through the many trials of life. While working on this project, I came to a deeper understanding of Jesus' words in John 15:5, "...apart from Me, you can do nothing."

At the home front, it is with the utmost love and devotion that I thank my wife Cheri for standing beside me for the last 11 years "for better and for worse." None of my professional successes, including this thesis, would have come to fruition without her love and encouragement. My children Katie, Ashley, David and Beth have also been a source of sheer joy in my life, helping me always to keep things in perspective. I am also grateful to have parents who still are involved in my life. I thank my father for the thought-provoking scientific discussions and my mother for the theological talks--both have offered continual encouragement over the years. I am also appreciative of my in-laws, who on many occasions have helped me to embrace an attitude of "think I can" rather than "think I can't." I am truly blessed for the God-given gift of family.

This thesis would *never* have materialized without the wisdom, determination and selflessness of two very devoted professors, Drs. Hampton N. Shirer and Robert Wells. As my primary thesis advisor (and perhaps the most patient man I know), Dr. Shirer was a continual source of encouragement and optimism. I recall numerous occasions when he "talked me in off the ledge" and provided the impetus to keep going, despite the many obstacles along the way. It has been a pleasure working with such a motivated and knowledgeable professional. Dr. Wells, who is also patient beyond human

comprehension, provided keen mathematical insights into improving the model and explained difficult mathematical concepts at a level I could understand. In addition to the mathematical insights, I shall always remember our philosophical and theological discourses--I only wish there were more. Thank you both for your commitment to excellence and for keeping students a priority despite your busy schedules.

I'd also like to thank Drs. Harry Henderson and Ray Masters for providing top-notch computer and graphics support throughout the course of my time at Penn State.

As far as peer support is concerned, I am eternally grateful to have shared an office with (soon to be) Dr. Nathaniel "Pete" Winstead, who provided meteorological and computer expertise, political insights, encouragement, laughter and most importantly, friendship. I shall never forget our quest for the perfect *Salvelinus fontinalis*. I also am grateful for the friendship and support offered by my Air Force comrades, Robert Williams, Mark Fitzgerald and Dan Pawlak. Finally, I'd like to thank my program manager, James Ulman, who has always "come through" when needed.

Chapter 1

INTRODUCTION

Since its civilian introduction nearly three decades ago, satellite- and aircraft-borne synthetic aperture radar (SAR) has become a viable instrument to aid the study of the marine atmospheric boundary layer (MABL). The potential usefulness of SAR to meteorology and oceanography was predicted by Vesecky and Stewart (1982), and SAR today continues to show great promise for MABL research, as recent studies suggest (e.g., Alpers and Brümmer 1994; Sikora *et al.* 1995; Mourad 1996).

SAR works by detecting variations in radar reflectance from the ocean surface (Thompson, *et al.* 1983). The backscatter patterns are generated by differences in surface roughness and are mapped to create high-resolution images. Wind-imposed stress is the primary mechanism for the generation of centimeter-scale capillary waves (Vesecky and Stewart 1982), and this wavelength magnitude corresponds to that which reflects waves via Bragg resonance scattering. Generally, SAR images depict high-stress regions as white and low-stress regions as black (see Sikora *et al.* 1995; for a high quality SAR image). In the absence of intense oceanographic and synoptic-scale atmospheric wave forcing phenomena, we may assume that the waves and resultant sea surface stress patterns are due almost entirely to smaller kilometer-scale atmospheric effects, namely secondary boundary layer circulations (Sikora *et al.* 1995). Therefore, SAR appears well suited to studying the wind variability caused by secondary circulations within the MABL. By proper interpretation of a SAR image, we can theoretically deduce the conditions in the MABL that create the observed stress patterns, as well as regions of convergence and divergence at the surface (Gerling 1986; Alpers and Brümmer 1994). Before employing SAR as a reliable remote sensing tool for the determination of surface layer wind speed

and direction, we must first fully understand the effects of MABL flows on the sea surface (Thompson *et al.* 1983). To accomplish this objective, here we model secondary circulations in the MABL and study their effects on modulating sea surface stress.

There are two major types of secondary boundary layer circulations that can develop and organize the sea surface stress patterns. The first comprises quasi-two-dimensional features, commonly referred to as boundary layer rolls; the second comprises three-dimensional flows, called boundary layer convective cells (Brown 1980). Three-dimensional cells may form independently of rolls when surface layer winds are light, or from rolls when thermal forcing is increased sufficiently (Woodcock 1940, 1975; Deardorff 1976). There are three principal instability mechanisms responsible for the formation of rolls and cells in the atmosphere: inflection point instability, parallel instability and thermal instability (Brown, 1980; Stensrud and Shirer, 1988; Etling and Brown, 1993). The first two draw energy from the background wind shear in the boundary layer (Faller 1965). The inflection point instability mechanism taps the normal component of the mean shear and satisfies the Rayleigh and Fjortoft conditions by requiring a point of inflection and a vorticity maximum within the background wind profile (Kundu 1990). Parallel instability draws energy from the parallel component of the mean shear via the Coriolis terms (Lilly 1966). Due to the length and time scales of the secondary flows under consideration, the parallel instability mechanism is of little consequence at our scale (Brown 1980). The third mechanism, thermal instability, derives its forcing from the air-sea temperature difference and can be likened to classic Rayleigh-Bénard convection. For consistency with Shirer *et al.* (1996), we refer to the rolls and cells as boundary layer convective eddies (BLCE). The vertical extent of the BLCE is given by the boundary layer depth, and their primary effect is the stabilization of the atmosphere through the transport of heat and momentum.

Numerous projects have been undertaken to model BLCE using nonlinear dynamical systems (e.g., Shirer 1986; Haack and Shirer 1992; Laufersweiler and Shirer 1995). The primary goal of these studies was to determine the temporal and spatial responses of BLCE to different forcing rates, both mechanical and thermal. These models successfully capture rolls and provide the fluxes of heat and horizontal momentum as well. However, due to the limitations imposed by the rigid, stress-free and perfectly conducting upper and lower boundary conditions, we are unable to use any of these models to deduce the role BLCE play in perturbing the sea surface, as is required to apply the remote sensing capabilities of SAR to the MABL.

To overcome this obstacle, Zuccarello (1994) developed, and Lambert (1995) later improved, a nonlinear, three-dimensional, Boussinesq model that provides for subgrid-scale momentum and heat fluxes at the lower boundary. Two constant forcing parameters are derived from Monin-Obukhov similarity theory to capture the flux contributions in the surface layer; these yield thermodynamic forcing and momentum dissipation. The new boundary conditions are more realistic and can be used to deduce wind-imposed stress on the sea surface. Following the success of Laufersweiler and Shirer (1995), Lambert introduced (after his 1995 work) an inversion layer into the model to cap moderately forced secondary circulations. However, we still specify the upper boundary to be rigid, stress-free and perfectly conducting, as was done in previous MABL models.

The initial results obtained by Zuccarello (1994) in his case study were encouraging, for they indicated that the model adequately captures the spatial characteristics of the MABL secondary circulations. Additionally, the component of the mean wind perpendicular to the roll axis (i.e., the cross-roll mean wind) and the period of the system reflect those that are typically observed in the atmosphere. However, Zuccarello did encounter several problems during his case study. One was the presence of an unknown energy source that prevented model equilibration during integration. The second was a

vertical velocity maximum that appeared at the lower boundary, instead of within the boundary layer at the typically reported height of 0.3 times the domain depth (Lenschow *et al.* 1980). Lambert (1995) conducted an energetics analysis and identified an extraneous kinetic energy source at the lower boundary of the model. By imposing two additional boundary conditions on the flow, he eliminated the unwanted energy source as well as the vertical velocity anomaly, enabling model integration and quasi-equilibration. Lambert also developed a subroutine to construct the model output and aid in the visualization of the model solution. The apex of his work was the creation of an x-y planview that depicts reasonable wind-imposed stress patterns on the sea surface.

The purpose of this study is to continue Zuccarello (1994) and Lambert's (1995) work on the impact BLCE have on sea surface stress, with an emphasis on visualization of the model solutions. In Chapter 2 we summarize background theory and model development, then review the system of partial differential equations and the spectral conversion. We conclude the chapter by describing the details of the computer model. In Chapter 3 we note improvements made to the model since Lambert's (1995) work, and in Chapter 4, we present case studies from the Hi-Res 2 field experiment (Lambert 1995; Sikora *et al.* 1995). We conclude by proposing areas for future research.

Chapter 2

MODEL OVERVIEW

Boundary layer convective eddies (BLCE) have been the focus of many studies in recent years. A number of these employ nonlinear dynamical systems to model kilometer-scale circulations (e.g., Shirer 1986; Haack and Shirer 1992; Laufersweiler and Shirer 1995). The motivation behind these studies has been to explain the temporal and spatial responses of BLCE to thermal and mechanical forcing mechanisms. Such models successfully capture the secondary circulations and provide the associated vertical flux profiles of heat and horizontal momentum--but *within* the boundary layer, not across the boundaries themselves. For simplicity, the upper and lower boundaries used in these models are rigid, stress-free and perfectly conducting. Hence, fluxes at or near the boundaries can not be adequately represented and the effects of BLCE on sea surface stress can not be deduced, as is required for the application of SAR technology to the study of the MABL.

Zuccarello (1994) develops a spectral model that incorporates nonzero subgrid-scale momentum and heat fluxes at the lower boundary, allowing the study of BLCE-induced sea-surface stress. In specifying the boundary conditions, he invokes similarity theory (Stull 1988). For simplicity and consistency with earlier models, Zuccarello keeps the upper vertical boundary rigid, stress-free and perfectly conducting. Lambert (1995) expands upon Zuccarello's work in several areas: he (a) conducted an energetics analysis to identify an extraneous energy source and vertical velocity anomaly at the lower boundary; (b) reformulated the lower boundary conditions to eliminate the problems in (a); and (c) developed an output subroutine to aid the analysis and interpretation of the

model solution, with an emphasis on the lower boundary stress planview for comparison with SAR. After finishing his thesis, Lambert incorporated an inversion subroutine into the computer model.

Here, we extend the work done by Zuccarello and Lambert on their BLCE model, focusing primarily on visualization of the model solutions.

2.1. Summary of Model Development and Background Theory

Zuccarello (1994) provides a detailed account of model development and background theory. Here, we summarize Zuccarello's work, as did Lambert (1995), and encourage interested readers to review his unabridged presentation. We have modified Zuccarello and Lambert's temperature base state to allow for the inclusion of an inversion and an unstable surface layer of the type used by Laufersweiler and Shirer (1995).

We employ the shallow Boussinesq system of equations to capture the convective nature of boundary layer secondary circulations. These circulations, manifested as two-dimensional rolls or three-dimensional cells, generally transport heat upward and horizontal momentum downward, while tending to alter the vertical shear in the boundary layer.

The basic, or conductive state, is considered to be time-independent, isopycnic, hydrostatic, incompressible and horizontally moving (Shirer 1986). It is represented by the standard meteorological variables with subscript 0 in the following equations:

$$\mathbf{v}_0(z) = \mathbf{V}(z) = U(z)\mathbf{i} + V(z)\mathbf{j} \tag{2.1}$$

$$\rho_0 = \rho_{00} \tag{2.2}$$

$$\theta_0(z) = \theta_{00} + \theta_h(z) \qquad (2.3)$$

$$p_0(z) = p_{00} - \rho_{00}gz, \qquad (2.4)$$

where the 00 subscript denotes atmospheric values at the bottom of the domain and $\theta_h(z)$ is the height-dependent portion of the temperature profile. We have rewritten the thermal base state using potential temperature $\theta_0(z)$, which is composed (in the model) of three different linear profiles in the surface layer, the neutral boundary layer and the inversion layer (Section 3.1). Moreover, the mean MABL density is essentially equal to the density at the sea surface (2.2).

We represent rolls and cells as perturbations superimposed on this basic state. Variables unique to the secondary circulation perturbations are denoted by primes in the following equations:

$$u'(x,y,z,t) = u(x,y,z,t) - U(z) \qquad (2.5)$$

$$v'(x,y,z,t) = v(x,y,z,t) - V(z) \qquad (2.6)$$

$$w'(x,y,z,t) = w(x,y,z,t) \qquad (2.7)$$

$$\rho'(x,y,z,t) = \rho(x,y,z,t) - \rho_{00} \qquad (2.8)$$

$$\theta'(x,y,z,t) = \theta(x,y,z,t) - \theta_0(z) \qquad (2.9)$$

$$p'(x,y,z,t) = p(x,y,z,t) - p_0(z). \qquad (2.10)$$

We have chosen the horizontal domain to be infinite and cyclically continuous, with gravest modes L_x and L_y, where L_x and L_y are the x and y domain lengths necessary to encompass one entire wavelength L of the circulation ($L^{-2} = L_x^{-2} + L_y^{-2}$). The vertical domain extends from the lower boundary, $h_{LB} = 10 \ m$ (anemometer height), to the cloud top height (z_T). Figure 2.1, which shows one half of the horizontal domain, clearly depicts

the secondary circulation as bounded by the base of the inversion z_i and h_{LB}. Since temperature decreases and wind speed increases with height, we can visualize in the air/sea interface layer how the net vertical heat flux at $z = h_{LB}$ should be positive and the net vertical transport of horizontal momentum should be negative.

We rewrite the entire domain in dimensionless form as $(0,0,0) \leq (x^*, y^*, z^*) \leq (1,1,1)$. The model is designed to capture the circulation above h_{LB} and employs surface layer similarity theory (Stull 1988) to parameterize the transport of heat and momentum below h_{LB} via the boundary conditions described in the next section.

MODEL BLCE CIRCULATION
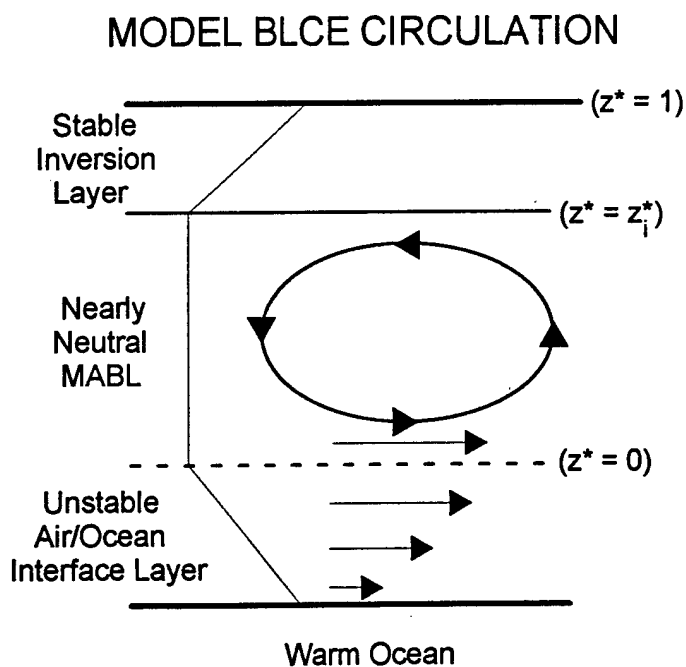
Fig. 2.1. A schematic cross section of a BLCE in the MABL, in which the air/ocean interface layer is greatly exaggerated. The air/ocean interface layer potential temperature decreases and the wind speed increases with height. The model domain extends from $z = h_{LB}$ ($z^* = 0$) to $z = z_T$ ($z^* = 1$) (Adapted from Shirer et al. 1996).

2.2. The System of Partial Differential Equations

In order to make our Boussinesq system of equations dimensionless, Zuccarello (1994) offers the following definitions:

$$\mathbf{v}'_H = \frac{\mathbf{v}_H^* \kappa}{z_T - h_{LB}} \tag{2.11}$$

$$w' = \frac{w^* \kappa}{z_T - h_{LB}} \tag{2.12}$$

$$x = x^* L_x \tag{2.13}$$

$$y = y^* L_y \tag{2.14}$$

$$z = z^* (z_T - h_{LB}) + h_{LB} \tag{2.15}$$

$$t = t^* \frac{(z_T - h_{LB})^2}{\kappa} \tag{2.16}$$

$$\theta' = \frac{\theta^* \nu \kappa \theta_{00}}{g(z_T - h_{LB})^3} \tag{2.17}$$

$$p' = \frac{p^* \rho_{00} \kappa^2}{(z_T - h_{LB}) L_x} \tag{2.18}$$

$$\mathbf{V}(z) = |\mathbf{V}(z_T)| \mathbf{V}^*(z^*) \tag{2.19}$$

$$f = \frac{f^* \kappa}{(z_T - h_{LB})^2} \tag{2.20}$$

$$\widetilde{\nabla} = a_x \frac{\partial}{\partial x^*} \mathbf{i} + a_y \frac{\partial}{\partial y^*} \mathbf{j} + \frac{\partial}{\partial z^*} \mathbf{k} , \tag{2.21}$$

where the constant thermal conductivity is represented by κ, the constant eddy viscosity by ν and the roll aspect ratios by a_x and a_y, defined below. We then eliminate pressure from the momentum equation by taking the curl to form a vorticity equation. Together with the thermodynamic and continuity equations, the resulting dimensionless system of equations is

$$\frac{\partial \theta^*}{\partial t^*} = \widetilde{\nabla}^2 \theta^* - Re\mathbf{V}^* \bullet \widetilde{\nabla}\theta^* - \frac{\partial \theta_0^*}{\partial z^*} w^* - \mathbf{v}^* \bullet \widetilde{\nabla}\theta^* \qquad (2.22)$$

$$\frac{\partial(\widetilde{\nabla} \times \mathbf{v}^*)}{\partial t^*} = P\widetilde{\nabla}^2(\widetilde{\nabla} \times \mathbf{v}^*) - f^* P\left[\widetilde{\nabla} \times (\mathbf{k} \times \mathbf{v}^*)\right] + P(\widetilde{\nabla} \times \theta^* \mathbf{k}) - Re\left[\widetilde{\nabla} \times (\mathbf{V}^* \bullet \widetilde{\nabla}\mathbf{v}^*)\right]$$

$$- \left[\widetilde{\nabla} \times (\mathbf{v}^* \bullet \widetilde{\nabla}\mathbf{v}^*)\right] - Re\left[\widetilde{\nabla} \times \left(w^* \frac{\partial \mathbf{v}^*}{\partial z^*}\right)\right] \qquad (2.23)$$

$$\widetilde{\nabla} \bullet \mathbf{v}^* = 0. \qquad (2.24)$$

In (2.22), Lambert (1995) chose $-(\partial \theta_0^* / \partial z^*) = Ra = -1$ to represent the background neutral boundary layer. We can therefore extract five dimensionless parameters from our system of equations--the eddy Prandtl number, P; the roll aspect ratios, a_x and a_y; the Reynolds number, Re; and the Rayleigh number, Ra. Their definitions are

$$P = \nu/\kappa \qquad (2.25)$$

$$a_x = \frac{(z_T - h_{LB})}{L_x} \qquad (2.26)$$

$$a_y = \frac{(z_T - h_{LB})}{L_y} \qquad (2.27)$$

$$Re = |\mathbf{V}(z_T)|(z_T - h_{LB})/\kappa \qquad (2.28)$$

$$Ra = -\frac{g\Delta_{BL}\theta(z_T - h_{LB})^3}{\nu\kappa T_{00}}, \qquad (2.29)$$

where $\Delta_{BL}\theta$ is the potential temperature difference across the boundary layer. The Reynolds number characterizes the dynamic forcing by the mean wind shear in the basic state, while the Rayleigh number represents thermodynamic forcing throughout the (nearly neutral) boundary layer.

For the dimensionless Boussinesq system of differential equations, we choose the horizontal domain to be cyclic and specify the upper vertical boundary to be rigid, stress-free and perfectly conducting. The lower boundary, however, is an important source of thermal energy for secondary circulation development and a sink for momentum (Fig. 2.1). In specifying lower boundary conditions, Zuccarello (1994) defines two parameters to control the forcing: the Schramm momentum constant, s_m, and the Schramm temperature constant s_T, both of which are positive, consistent with Figure 2.1. The upper and lower boundary conditions are

$$\theta^*(1) = 0 \tag{2.30}$$

$$\frac{\partial u^*(1)}{\partial z^*} = \frac{\partial v^*(1)}{\partial z^*} = w^*(1) = 0 \tag{2.31}$$

$$\theta^*(0) + s_T \frac{\partial \theta^*(0)}{\partial z^*} = 0 \tag{2.32}$$

$$u^*(0) - s_m \frac{\partial u^*(0)}{\partial z^*} = 0 \tag{2.33}$$

$$v^*(0) - s_m \frac{\partial v^*(0)}{\partial z^*} = 0 \tag{2.34}$$

$$\frac{\partial w^*(0)}{\partial z^*} - s_m \frac{\partial^2 w^*(0)}{\partial z^{*2}} = 0. \tag{2.35}$$

Note that (2.35), which follows from (2.32) and (2.34) via the continuity equation, is not ideal in that it involves derivatives of the vertical velocity w^* at the lower boundary, instead of w^* itself. In early model runs, this anomaly manifested itself by producing vertical velocity maxima at the lower boundary, instead of the more physically reasonable $w^* = 0$. To overcome this obstacle, Lambert (1995) introduces two new boundary conditions:

$$w^*(0) = 0 \tag{2.36}$$

$$\mathbf{A}^*(0) = 0, \tag{2.37}$$

where $\mathbf{A}^*$ is the vector streamfunction defined in the following section. In the atmosphere, the BLCE vertical velocity perturbation at $h_{LB} = 10\ m$ ($z^* = 0$) is not identically zero, but to an excellent approximation we may regard it as such.

To attain boundary conditions (2.36) and (2.37), Lambert (1995) redefines the vertical streamfunction basis functions instead of rewriting the entire model. For a complete account of this procedure, we refer the reader to Appendix B of his work.

2.3. From Differential Equations to Computer Code: The Spectral Conversion

To create a spectral model from our system of partial differential equations (PDEs), Zuccarello (1994) employs the Galerkin technique or spectral method (Higgins 1987). When applied to the vorticity (2.23) and thermodynamic (2.22) equations, this method yields a nonlinear dynamical system (NDS). Originally, the NDS consisted of 60 equations--20 for temperature and 40 for streamfunction--but was reduced to 50 when Lambert (1995) introduced new lower boundary conditions (2.36) and (2.37). The new NDS still has 20 equations for temperature but now has only 30 for streamfunction.

Since the velocity perturbation vector $\mathbf{v}^*$ is nondivergent, it can be represented by the curl of a vector streamfunction $\mathbf{A}^*$, whose components are ψ^* and η^* in the x^*- and y^*- directions, respectively:

$$\mathbf{v}^* = \nabla \times \mathbf{A}^* = \nabla \times (\psi^* \mathbf{i}) + \nabla \times (\eta^* \mathbf{j}). \tag{2.38}$$

Truncated Fourier expansions for θ^*, ψ^* and η^* are composed of time-dependent amplitudes, spatially-dependent trigonometric functions with horizontal wavenumbers l and m, and vertical basis functions, $F_j(z^*)$ and $h_q(z^*)$:

$$\theta^*(x^*,y^*,z^*,t^*) = \sum_{i=0}^{4}\sum_{j=1}^{4} \theta_{ij}(t^*) trig_i(x^*,y^*) F_j(z^*) \tag{2.39}$$

$$\psi^*(x^*,y^*,z^*,t^*) = \sum_{p=0}^{4}\sum_{q=1}^{3} \psi_{pq}(t^*) trig_p(x^*,y^*) h_q(z^*) \tag{2.40}$$

$$\eta^*(x^*,y^*,z^*,t^*) = \sum_{p=0}^{4}\sum_{q=1}^{3} \eta_{pq}(t^*) trig_p(x^*,y^*) h_q(z^*), \tag{2.41}$$

where

$$trig_0(x^*,y^*) = 1 \tag{2.42}$$

$$trig_1(x^*,y^*) = \sin 2\pi l x^* \sin 2\pi m y^* \tag{2.43}$$

$$trig_2(x^*,y^*) = \sin 2\pi l x^* \cos 2\pi m y^* \tag{2.44}$$

$$trig_3(x^*,y^*) = \cos 2\pi l x^* \sin 2\pi m y^* \tag{2.45}$$

$$trig_4(x^*,y^*) = \cos 2\pi l x^* \cos 2\pi m y^*. \tag{2.46}$$

Here the orthogonal θ^* vertical basis functions are

$$F_1(z^*) = \cosh \omega_1 z^* - \frac{1}{s_T \omega_1} \sinh \omega_1 z^* \quad \text{for } s_T < 1 \tag{2.47}$$

$$F_1(z^*) = \cos \omega_1 z^* - \frac{1}{s_T \omega_1} \sin \omega_1 z^* \quad \text{for } s_T > 1, \tag{2.48}$$

where

$$s_T \omega_1 = \tanh \omega_1 \quad \text{for } s_T < 1 \tag{2.49}$$

$$s_T \omega_1 = \tan \omega_1 \quad \text{for } s_T > 1, \tag{2.50}$$

and

$$F_j\left(z^*\right) = \cos\omega_j z^* - \frac{1}{s_T \omega_j}\sin\omega_j z^* \quad \text{for} \quad j = 2,3,4, \tag{2.51}$$

where

$$s_T \omega_j = \tan\omega_j \quad \text{for} \quad j = 2,3,4. \tag{2.52}$$

The nonorthogonal ψ^* and η^* vertical basis functions are expressed as differences:

$$h_q\left(z^*\right) = \left(\cos\varpi_q z^* - s_m\varpi_q \sin\varpi_q z^*\right) - \left(\cos\varpi_{q+1} z^* - s_m\varpi_{q+1}\sin\varpi_{q+1} z^*\right) \quad \text{for} \quad q = 1,2,3, \tag{2.53}$$

where

$$s_m\varpi_c = \cot\varpi_c \quad \text{for} \quad c = 1,2,3,4. \tag{2.54}$$

To produce our NDS (2.39) - (2.41) using the standard Galerkin procedure (Higgins 1987), we insert the θ^*, ψ^* and η^* expansions into the dimensionless PDEs multiplied by the corresponding basis functions, and integrate over the domain (Shirer 1987). Appropriate trigonometric identities are applied to simplify the resulting terms in the equations.

In the NDS, each PDE term is represented as the product of a 50 X 50 matrix and a 50-element amplitude coefficient vector, allowing us to write the model equations in the form:

$$A\dot{y} = By + C(y)y, \tag{2.55}$$

where A is a 50 X 50 invertible matrix of inner products; B is a 50 X 50 constant linear matrix, determined by P, Re, Ra, a_x, a_y and the Fourier coefficients of the background temperature and wind; and C is a 50 X 50 linear-in-y matrix from the advective terms of the two systems of PDEs. The 50-element column vector y contains 20 time-dependent

spectral amplitudes for temperature, T_{ij}, and 30 time-dependent spectral amplitudes for the streamfunction components, ψ_{pq} and η_{pq}. The 50-element column vector $\dot{y}$ represents the temporal derivatives of the spectral amplitudes in y. Since A is invertible, we may rewrite (2.55) in the form

$$\dot{y} = A^{-1}By + A^{-1}C(y)y. \qquad (2.56)$$

This is the form used in the numerical integration.

2.4. The Computer Model

The physical and mathematical model described in the preceding sections was encoded by Zuccarello (1994) using the FORTRAN programming language; it was originally compiled with a UNIX-based WATFOR77 compiler. To add portability, flexibility and ease of operation, we developed a PC version of the code using Microsoft's *Fortran Power Station 4.0* software. Code editing, compilation and execution are now done easily.

The sequence of steps necessary to carry out a SAR analysis using the model are summarized by the flowchart in Figure 2.2 and are referenced periodically throughout the text that follows. As with any study, we first select a case (Figure 2.2, Step A) and specify atmospheric input parameters like those shown in Table 4.1.

Using a subroutine discussed in Appendix A of Zuccarello (1994), we input the wind speed and mixing ratio at 10 m as well as the air-sea temperature difference, and employ Monin-Obukhov surface layer similarity theory to determine values for the Schramm momentum and temperature constants, s_m and s_T (Figure 2.2, Step B). Based upon these

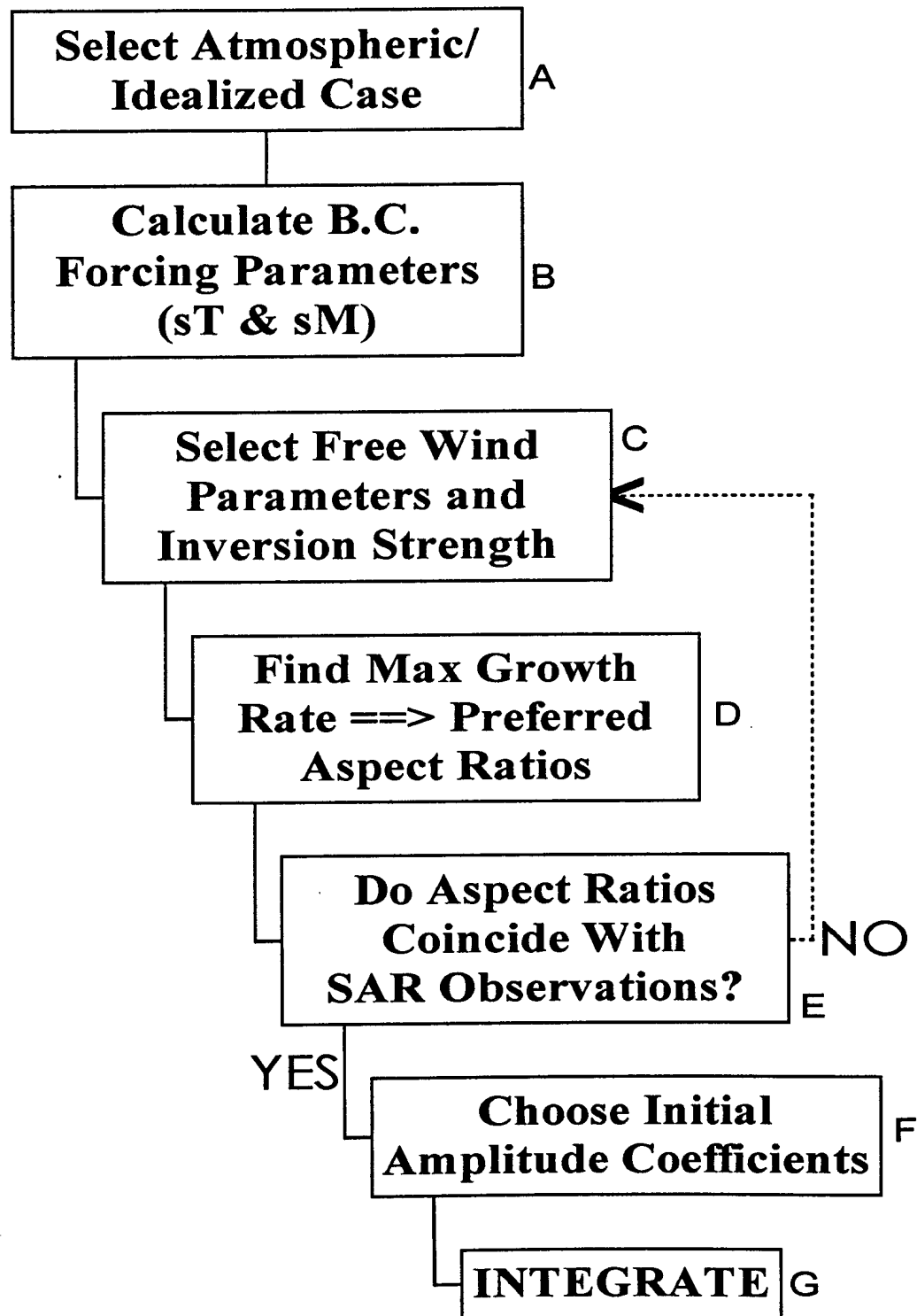Fig. 2.2. Summary of required steps in a SAR analysis.

input values, the code calculates values for ω_j and ϖ_c, where $j,c = 1,2,3,4$, and then iteratively solves (2.49), (2.50), (2.52) and (2.54) for the eigenvalues. Lambert (1995) empirically derives a single set of initial ω_j and ϖ_c values for this iterative process that works well for most cases. However, for certain values of s_m and s_T, we encounter problems, suggesting that ω_j and ϖ_c are jumping to other quadrants of their respective tangent and cotangent functions; this phenomenon causes an undesirable convergence to previously determined omega values. To correct this problem, we choose seed values that are multiples of π for ω_j, and multiples of $\pi/2$ for ϖ_c; for the case $s_T < 1$, we set $\omega_1 = (s_T)^{-1}$. Then we apply the bisection method to approximate each ω_j, ϖ_c, thus obtaining initial values for the Newton's method iteration scheme. Extensive testing has demonstrated the reliability of this automated eigenvalue routine.

We next construct a background wind profile using the four free parameters: $U(z_T)$, $V(z_T)$, d_U and d_V (Figure 2.2, Step C). The former two are chosen by the user to control the overall speed and turning shear in the profile, while the latter two are the free constants in the wind profile equations:

$$U(z) = a_U z + b_U z^{2/3} + c_U z^{1/3} + d_U \qquad (2.57)$$

$$V(z) = a_V z + b_V z^{2/3} + c_V z^{1/3} + d_V . \qquad (2.58)$$

We apply (2.15) and (2.19) to nondimensionalize these profile equations and then require the mean background wind profiles to satisfy the same boundary conditions as the perturbation wind velocities do. These boundary conditions are

$$U^*(z^* = 0) - s_m \frac{\partial U^*(z^* = 0)}{\partial z^*} = 0 \qquad (2.59)$$

$$V^*\left(z^* = 0\right) - s_m \frac{\partial V^*\left(z^* = 0\right)}{\partial z^*} = 0 \ . \tag{2.60}$$

Additionally, we must specify $U(z^* = 0)$ and $V(z^* = 0)$, which are the same boundary values used to calculate the Schramm momentum constant s_m. As a result of our nondimensionalization definition (2.19), we note that the following condition is also met:

$$\left| \mathbf{V}^*(z^* = 1) \right| = 1 \ . \tag{2.61}$$

Because (2.61) is not a new boundary condition, we are left with six equations and eight unknown variables, two of which are the free wind parameters d_U and d_V. Lambert (1995) developed an EXCEL spreadsheet to enable users to easily find the values for d_U and d_V necessary to give physically realistic background wind profiles. Figure 2.3 shows an example of how the wind profile speed changes by altering the values of d_U and d_V. For this scenario, we experiment until we arrive at the best possible wind profile for the given atmospheric conditions--curve B in Figure 2.3. This plausible boundary layer background wind profile corresponds to $d_U = 4.1$ and $d_V = 1.5$ when $|\mathbf{V}(h_{LB})| = 4$ m/s and $|\mathbf{V}(z_T)| = 8$ m/s. Wind direction profiles, though not shown, are determined concurrently with the speed profiles. Before moving from Step C to Step D in Figure 2.2, we must specify a plausible inversion strength (^{0}C/m), preferably from an atmospheric sounding.

A linear stability analysis (Figure 2.2, Step D) is then performed to determine what domain shape, specified by L_x and L_y, yields the largest growth rates for a given domain depth z_T--these are the modes we would expect to observe in the atmosphere (Laufersweiler 1987). With the assistance of a contouring software package, we can readily identify the fastest growing mode and its corresponding a_x and a_y values, the preferred aspect ratios. Before integrating our system of equations, we determine a set of

BACKGROUND WINDSPEED

- - - - - du = 3.1; dv = 0.5 (A)

———— du = 4.1; dv = 1.5 (B)
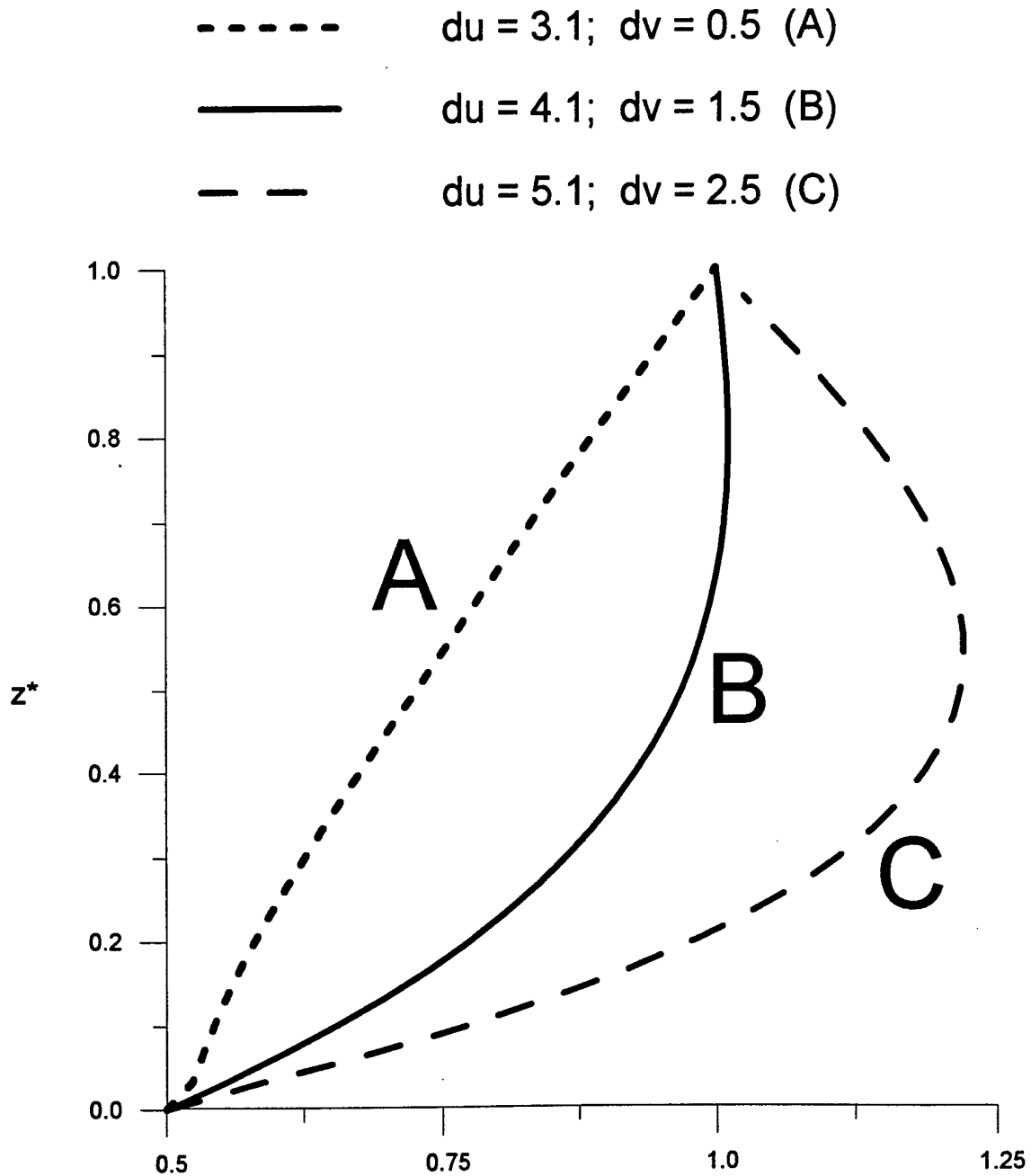
— — du = 5.1; dv = 2.5 (C)

Fig. 2.3. Dimensionless wind speed profiles as determined by the mean background wind parameters, d_U and d_V. Note how the wind speed profile changes from A to C as d_U and d_V are incremented by 1.0. We find d_U and d_V empirically to attain more physically plausible wind profiles. Here, we choose profile B.

initial conditions for the 50-element vector y using the eigenvectors associated with the eigenvalues ω_j and ϖ_c (Figure 2.2, Step F). If we desire a continuation run, then we use y-vector values from the end of the previous integration.

Matrix A and matrix B (2.55), which represent the temporal-derivative terms and all other linear terms, respectively, are determined prior to integrating because they do not depend on the spectral coefficients y. In contrast, the nonlinear term matrix C is a linear function of y and must be recomputed at each integration time step, at least in theory. With efficiency in mind, Lambert (1995) re-expresses the linear function $C(y)$ using a cubic tensor of coefficients (CCUBE, Section 3.2) so that these need not be recomputed at each time step. Of course, the same shortcut applies to the coefficient term $A^{-1}C(y)$ in (2.56). We use the IMSL subroutine DLINRG to convert matrix A into A^{-1}, employ DMRRRR to determine $A^{-1}B$, and calculate $A^{-1}C$ directly.

Earlier versions of the model utilized the IMSL subroutine DIVPAG to perform the integration (Figure 2.2, Step G), with acceptable results for short (i.e., less than 32,000 time step) runs. For longer runs, however, we encountered eigenvalue convergence problems and numerical noise, suggesting that another integration scheme is necessary (Section 3.2). Since our system of equations is stiff, we adopted the semi-implicit integration scheme STIFBS from Press *et al.* (1992). Though not as fast as DIVPAG, STIFBS has greatly abated the noise and convergence problems, yielding smooth, consistent integrations.

We allow the model to integrate until the dimensionless energy ($y^T A y$) quasi-equilibrates. After the last integration time step, the model passes the time-dependent

amplitude coefficients to a computation/output (CO) subroutine developed by Lambert (1995), where the solution is constructed using (2.38)-(2.41). We have enhanced Lambert's CO subroutine by offering additional, more automated options.

In Chapter 4, we offer examples of model solutions generated by the CO subroutine for the Hi-Res 2 field experiment. Before doing so, however, we proceed to the next chapter where we expound the improvements made to the model since Lambert (1995).

Chapter 3

MODEL IMPROVEMENTS

At the onset of this study, we had hoped to immediately resume work on the interpretation of a SAR image taken during Hi-Res 2, a 1993 MABL field experiment conducted off the coast of North Carolina (Lambert 1995; Sikora *et al.* 1995). However, early model runs using Hi-Res 2 observations as input parameters were quite discouraging. In addition to very high frequency noise problems in the energy, streamfunction and temperature perturbations, we also observed startling dimensionless energy growth rates that terminated model runs prematurely. We experimented with altered initial conditions and subroutines to limit numerical roundoff errors with little or no effect, convincing us that further model improvements and debugging were necessary. We also were compelled to address previously unexplained numerical issues related to our NDS. Therefore, before pursuing the Hi-Res 2 case study further, we had to address model limitations and make corrections and modifications as necessary.

Preliminary troubleshooting revealed that the immense growth rates were due to the terms represented by the linear buoyancy matrix, and that the noise problem was generated by several sources, two of which were 1) the integration of stiff equations with a non-stiff numerical integration routine (Press *et al.* 1992), and 2) the nonlinear cubic tensor arising from the advection of vorticity (Section 2.4). Since this growth rate problem generally caused the computer code to crash, we decided to focus on the linear portion of the model first.

3.1. Addressing Monotonic Energy Growth

While constructing the model, Zuccarello (1994) built all the linear matrices *analytically* using the DERIVE software package. After completing his 1995 case study, Lambert did likewise when he constructed the inversion subroutine, the terms of which he merely added to those representing the neutral boundary layer (i.e., $Ra = -1$), as shown in the equation

$$\frac{\partial \theta_0^*}{\partial z^*} = -Ra + \frac{\partial \theta_i^*}{\partial z^*}. \tag{3.1}$$

In order to perform a completely independent cross-check of the linear buoyancy matrix, we began with the spectral representations for θ^*, ψ^* and η^* (2.39)-(2.41), encoded our own functions and integrated the results *numerically*. Since the trigonometric functions (2.42)-(2.46) are independent of z^*, and the basis functions (2.47)-(2.52) are independent of x^* and y^*, we were able to compute the x^*, y^*, z^* triple integral as a product of a double integral in x^*, y^* and a single integral in z^*. We used the IMSL subroutine DTWODQ for the double integral and DQDAG for the single one.

The analytic and numeric approaches to calculating the inversion were nearly identical, indicating that the inversion subroutine had been coded correctly. However, a closer examination of the analytically derived neutral boundary layer revealed unexplained errors. In the interest of time, we chose to incorporate the numerical subroutine into the model rather than to reformulate the analytic equations. This decision had the added benefit of making future modifications of the temperature profile more easy to implement.

After fully incorporating the numerically determined temperature profile, however, we found that the introduction of an inversion still tended to *increase* the overall energy of the

system, even with very weak inversions. The culprit appeared to be the dimensionless inversion lapse rate term

$$\frac{\partial \theta_i^*}{\partial z^*} = (\frac{\partial \theta_i}{\partial z})(\frac{g(z_T - h_{LB})^4}{\theta_{10} \upsilon \kappa}),$$ (3.2)

whose immense magnitude (of order 10^6) dominated all other terms in the NDS, especially those of the background temperature modification θ_{0j} (2.39). Adding an inversion to a thermally neutral boundary layer (of order unity) tended to throw the model solution out of balance, yielding colossal growth rates in the dimensionless energy.

Hoping to counteract this aphysical growth and yield more balanced solutions, we introduced an unstable surface layer that spreads the air-sea temperature difference over a user-specified surface layer depth (Laufersweiler and Shirer 1995); this yields a lapse rate term of similar magnitude to (3.2). The new potential temperature profile is similar to the one depicted in Figure 3.1, although the depth of the unstable surface layer has been exaggerated somewhat. The three lapse rates are, by definition, negative in the surface layer, slightly positive in the boundary layer and positive in the inversion layer. Quantitatively, the dimensional potential temperature lapse rates can be represented by the following equations:

$$\frac{\partial \theta_{SL}}{\partial z} = \frac{\Delta_{SL}\theta}{(z_{SL} - z_{h_{LB}})} \quad \{h_{LB} < z \le z_{SL}\}$$ (3.3)

$$\frac{\partial \theta_{BL}}{\partial z} = \frac{\Delta_{BL}\theta}{(z_i - z_{SL})} \quad \{z_{SL} < z \le z_i\}$$ (3.4)

$$\frac{\partial \theta_{IN}}{\partial z} = \frac{\Delta_{IN}\theta}{(z_T - z_i)} \quad \{z_i < z \le z_T\},$$ (3.5)
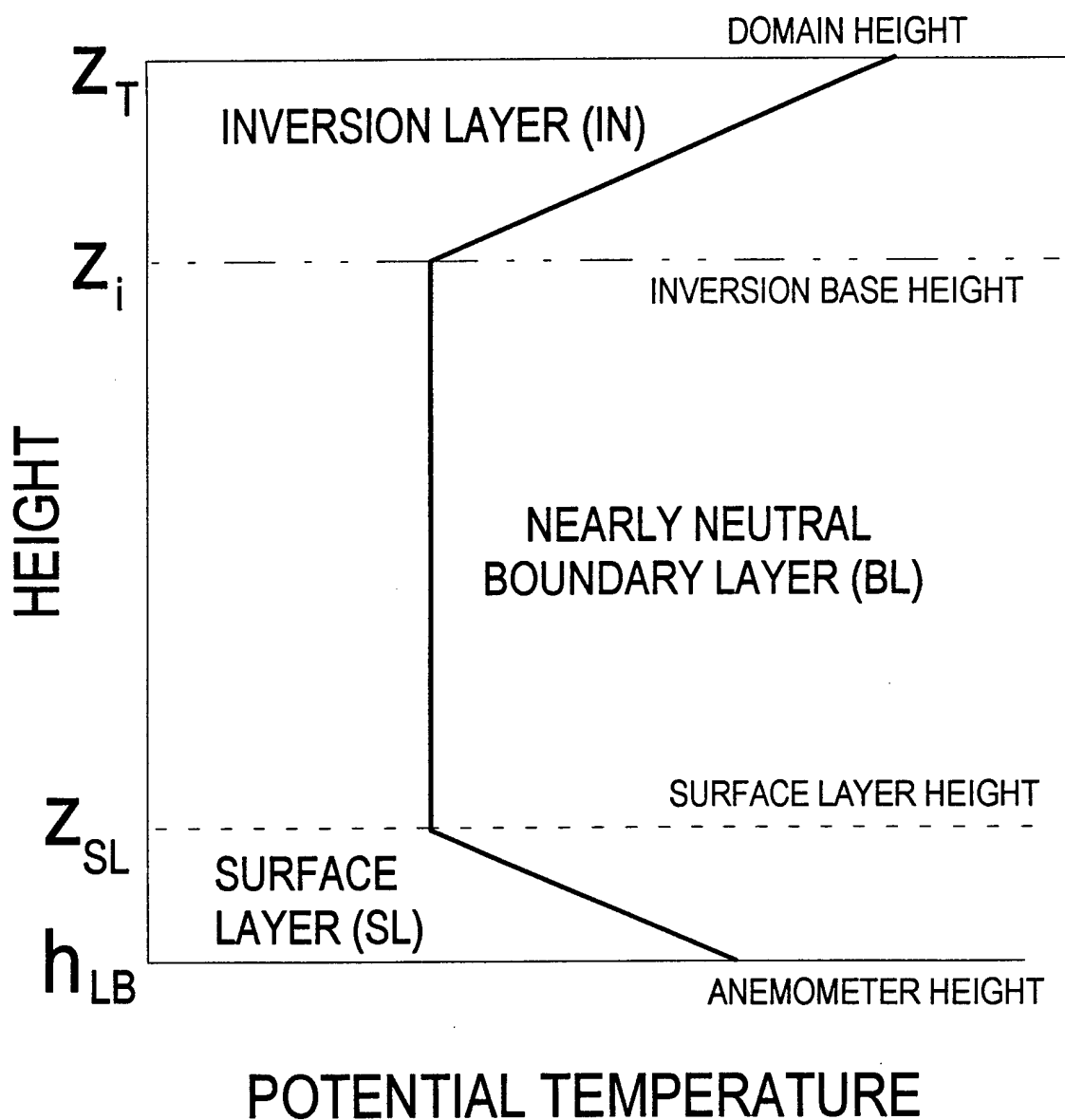
THERMAL BASE STATE

Figure 3.1. A schematic of the background potential temperature profile used in the model. (Not drawn to scale.)

where z_{SL} is the top of the unstable surface layer and $\Delta_n\theta$ is the change in potential temperature over the specified layer, n. All other variables are as defined in Chapter 2. This addition to the model did increase the magnitude of the other buoyancy terms as desired but did not completely balance the model solutions as we had hoped--there was still evidence of monotonic energy growth in several instances. We therefore added a nonlinear numerical dissipation term to bound the energy growth, without altering the linear growth rates or the preferred aspect ratios. Equation (2.56) now takes the form:

$$\dot{y} = A^{-1}By + A^{-1}C(y)y - d|y|y, \tag{3.6}$$

where d is an empirically determined dissipation coefficient; we use $d = 0.1$ for our study. Model runs with an inversion and surface layer now provide more stable, physically plausible results.

3.2. Addressing Numerical Noise

Isolating the source of numerical noise in the nonlinear terms proved to be less straightforward because the problem did not occur all the time. Model output showing the emergence of noise was extremely dependent on initial conditions, leading us to consider the possibility that the solution was chaotic (Lorenz 1993). As it turned out, such was not the case.

In the computer model (Section 2.4), there is a 50 X 50 X 50 matrix, CCUBE, that is used to calculate the $C(y)y$ term in (2.56). This cubic matrix holds the constant coefficients for the nonlinear temperature and streamfunction advective terms. Numerous diagnostic tests revealed that several CCUBE assignment statements contained indexing errors that manifested themselves as noise in the model solution. After Drs. Hampton Shirer and Robert Wells tediously re-indexed the CCUBE matrix, we noted vast

improvements in the model solution: the nonlinear terms became energy preserving as they should and numerical noise was minimized, occurring less frequently. However, these changes did not totally eradicate numerical noise from the model output as we would have liked, for during longer integrations when surface winds were light, noise continued to dominate the solution. The installation of a time filter reduced the amplitude of the fluctuations somewhat but did not remove the higher-frequency oscillations.

As noted in Chapter 2, we encountered eigenvalue convergence problems while using the integration subroutine DIVPAG. This experience alerted us to the possibility that the venerable IMSL subroutine might be the source of the numerical noise we were observing. Due to the gracious assistance of Prof. John Lopez of the Mathematics Department, Pennsylvania State University, we found that DIVPAG was not designed to handle a NDS of the type used by our model; nor was it reliable in working with stiff systems of equations, which are systems "where there are two or more very different scales of the independent variable on which the dependent variables are changing" (Press *et al.* 1992). We therefore implemented the *Numerical Recipes* semi-implicit integration subroutine STIFBS (Press *et al.* 1992), and we were pleased that model integrations became smoother and more consistent, not suffering eigenvalue convergence woes.

To attain the superior quality solutions afforded by STIFBS, however, there was a significant tradeoff in time. The new integration subroutine is considerably slower than DIVPAG (nearly five times slower for some cases) and this sluggishness hindered research progress. To alleviate this, we implemented a scheme to rescale the potential temperature perturbation terms so they more closely matched the magnitude of the vorticity terms. This improved the balance of our NDS solutions by reducing the number of iterations required at each integration time step, thereby increasing the overall speed of model runs without affecting the linear stability results. To incorporate this time-saving routine, we redefined a new potential temperature perturbation:

$$\theta'_{(new)} = s_f \theta'_{(old)}, \tag{3.7}$$

where s_f is the scale factor coefficient. Instead of tediously multiplying every individual matrix in the thermodynamic equation by s_f, we simply multiplied the first twenty elements of the vector y (the potential temperature elements) by s_f. To then balance the equations, we only had to multiply the buoyancy matrix D in the thermodynamic equation by s_f and the buoyancy matrix G in the vorticity equation by $(s_f)^{-1}$. After integrating with these alterations, we rescale all terms to their original size to construct the model solution. To our pleasure, the quality integrations given by STIFBS can now be achieved in about half the time.

We are now ready to use the model to study very large eddy circulations of the MABL. In Chapter 4, we resume work on the Hi-Res 2 case study.

Chapter 4

CASE STUDY

Since several significant alterations have been made to the model since its last major evaluation (Lambert 1995), we now ascertain whether the model solutions adequately represent observed atmospheric phenomena. To do so, we compare and contrast our numerical results with observations and synthetic aperture radar (SAR) imagery taken during the Hi-Res 2 field study, which is described in great detail by Sikora *et al.* (1995) and Lambert (1995).

We perform the sequence of steps outlined in Figure 2.2 and Section 2.4 to arrive at a numerical solution for the case under investigation. When trying to capture via a linear analysis the observed aspect ratios for an atmospheric (as opposed to idealized) case, we may use the "NO" loop in Figure 2.2 many times to re-select free wind parameters and/or the inversion strength. We iterate through this loop until both of the preferred aspect ratios a_x and a_y match the observed ones within ± 0.1 (which amounts roughly to a 10 percent error), the specified error of the SAR image spectral analysis for Hi-Res 2 (Shirer *et al.* 1997). After a successful linear analysis, we determine the parameter values of the model using Hi-Res 2 surface data, then perform and analyze nonlinear integrations using several different scale factor values s_f in (3.7). This has the effect of changing the impact of the nonlinear dissipation during the integration without altering the linear results; however, the effect on the model solution is substantial, as we demonstrate in Section 4.2. We begin in Section 4.1 by briefly describing Hi-Res 2 observations.

4.1. Overview of Hi-Res 2 Field Experiment and Data

The observational data used for this case study are from the Hi-Res 2 field experiment conducted in June 1993 off the coast of North Carolina, and they are reported by Sikora *et al.* (1995) and Lambert (1995). From 16 - 18 June 1993, two ships, the R/Vs *Columbus Iselin* and *Bartlett*, took observations at the sea surface and at $z = 10$ m within the region 35.2^0 - 36.6^0 N latitude and 73.8^0 - 75.0^0 W longitude. On 17 June 1993, the Hi-Res 2 MABL measurement region coincided with that imaged by the SAR on the European Remote Sensing Satellite (ERS-1). For this case study, we choose a composite image that was taken at 1538Z and was published by Sikora *et al.* (Figure 1, 1995).

According to Sikora *et al.* (1995), there are two distinct patterns present on the 17 June 1993 SAR image: a marbled pattern in the northwest portion and a mottled pattern throughout the southeast portion. The transition between these two regions occurs at the Gulf Stream North Wall (GSNW). The marbled region north of the GSNW is the SAR signature of a stable MABL, while the mottled region south of the GSNW is the signature of a thermally unstable MABL. Because we wish to study secondary circulations of the MABL induced by thermal and/or inflection point instabilities, we focus our study on the mottled region of the SAR image, specifically in the vicinity of 35.8^0 N, 74.2^0 W, where there are discernible kilometer-scale alternating dark/light patterns. About the time the SAR image was taken, the R/V *Columbus Iselin* was in the area and recorded surface observations that are summarized in Table 3.1 of Lambert (1995). As depicted by Table 4.1, we regroup the 17 June 1993 data into two sets, Sonde 1 and Sonde 2, based upon the times in which the ship was near the location of each launch. Sonde 1, which was launched at 1517Z, represents the time-averaged data from 1437Z - 1602Z, while Sonde 2, which was launched at 1955Z, represents the time average from 1941Z - 2241Z. Unfortunately, boundary layer sounding winds were unavailable for either data set; however R/V *Columbus Iselin* researchers reported that winds were relatively light

Table 4.1. Hi-Res 2 observational data. Sonde 1 denotes data averaged between 1437Z and 1602Z, and Sonde 2 denotes data averaged between 1941Z and 2241Z; both are from 17 June 1993. For our study, we use the Sonde 1 case. (R/V *Columbus Iselin* data courtesy of Dr. Jim Edson, Woods Hole Oceanographic Institution; SAR feature wavelengths courtesy of Dr. Todd Sikora, John Hopkins Applied Research Lab.)

OBSERVED VARIABLES	SONDE 1		SONDE 2	
	INVERSION	NO INVERSION	INVERSION	NO INVERSION
L_x (Rel. to East, m)	842	842	1714	1714
L_y (Rel. to North, m)	699	699	856	856
z_i (m)	409	--	930	--
z_T (m)	609	609	1180	1180
$\Delta_{IN}\theta$ (°C)	0.4	--	1.0	--
Target a_x	0.7	0.5	0.7	0.5
Target a_y	0.9	0.6	1.4	1.1
10m Wind Speed (m/s)	1.75	1.75	4.92	4.92
10m Wind Direction (°)	256	256	212	212
Current Speed (m/s)	1.57	1.57	1.69	1.69
Current Direction (°)	224	224	228	228
Rel. Wind Spd. (m/s)	0.93	0.93	3.33	3.33
Rel. Wind Dir. (°)	319	319	204	204
T_{10} (°C)	24.9	24.9	25.5	25.5
T_{00} (°C)	27.8	27.8	28.0	28.0
Mixing Ratio (g/kg)	13.6	13.6	14.5	14.5

throughout the boundary layer. Here, we use the Sonde 1 case for our study because it was closer to the time of the SAR image, and we propose that future work include an analysis of the Sonde 2 case.

The surface analysis shown in Figure 2 of Sikora *et al.* (1995) depicts the synoptic conditions at 1500Z on 17 June 1993. Aside from a mesofront near the GSNW (noted by the crew of the R/V *Columbus Iselin*), the meteorological conditions in the region of interest were relatively quiescent: only light winds and boundary layer cumulus were reported. This lack of appreciable synoptic-scale features suggests that boundary layer convective eddies (BLCE) were responsible for the stress patterns observed on the 1538Z SAR image in the region of interest for this study (Sikora *et al.* 1995).

The current-relative winds at 10 m for the Sonde 1 case were 0.93 m/s from 319^0 and the air-sea temperature difference was -2.9 ^{0}C (i.e., sea warmer than air). When plotted on a Woodcock (1975) diagram (Point A, Figure 4.1), the data fall into the three-dimensional regime. We therefore expect our model solution for this particular case to be cellular.

4.2. Case Study Analysis

We begin our investigation by determining the values of the lower boundary Schramm forcing parameters, s_T and s_m (Figure 2.2, Step B) for the Sonde 1 data. Using the subroutine described in Appendix A of Zuccarello (1994), we input the physical parameter values from Table 4.1 to obtain $s_T = 1.95$ and $s_m = 0.67$.

We then conduct an eigensystem linear analysis to determine the preferred values of the aspect ratios, which yield the shape of the horizontal domain by (2.26) and (2.27). For the given input parameter values, we iterate through a range of relevant a_x and a_y values,
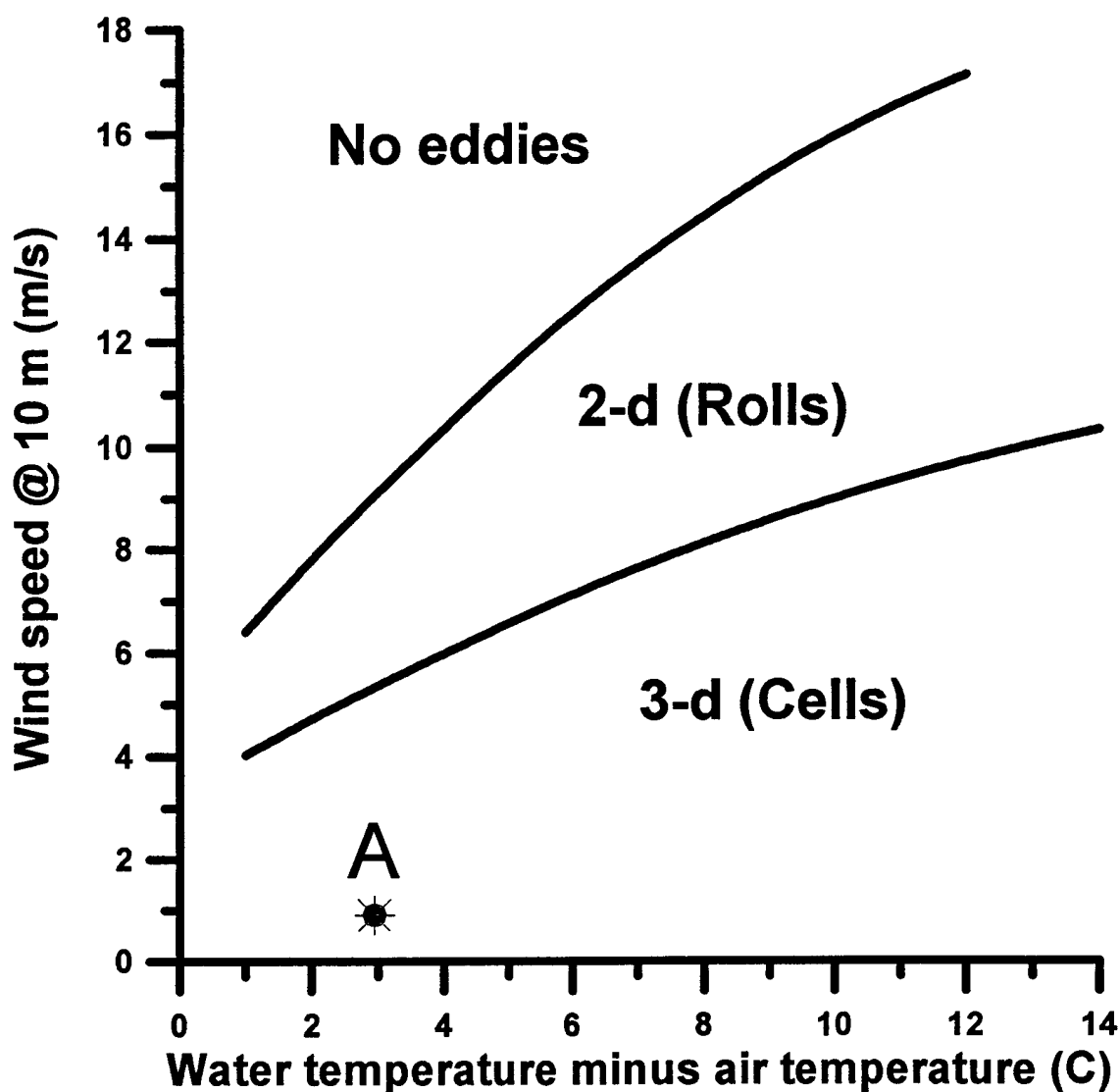
Woodcock (1975)

Figure 4.1. The Woodcock (1975) diagram predicts secondary circulation regimes from the current-relative wind speed at 10 m ($z^* = 0$) and the air/sea temperature difference. Point A represents the input observations from the Hi-Res 2 case study (Sonde 1).

then contour the real parts of the 50th eigenvalue (because the eigenvalues are sorted in ascending order by the value of their real parts). The aspect ratio region in which the largest positive real parts (or growth rates) are observed determines the preferred aspect ratios (Laufersweiler 1987). While invoking the "NO" loop in Figure 2.2, we adjust the free wind parameter values, inversion strength and/or surface layer depth, and re-iterate through the appropriate a_x and a_y values until we approach the values of the observed aspect ratios. We found during our study that this may not be possible for all cases in a reasonable amount of time. Fortunately for this present study, after increasing $\Delta_{IN}\theta$ from 0.4 ^{0}C (Table 4.1) to 1.8 ^{0}C, we were able to obtain acceptable aspect ratio values; the linear stability analysis plot in Figure 4.2 yields preferred aspect ratios, a_x and a_y, that are equal to 0.7 and 0.8, respectively. Shirer $et\ al.$(1997) conducted a spectral analysis of the 1538Z SAR image and found $a_x = 0.7 \pm 0.1$ and $a_y = 0.9 \pm 0.1$, as reported in Table 4.1. Because our findings are within the error tolerances of the spectral analysis, we may conclude that our NDS is capable of capturing the preferred horizontal wavelengths of the convective structures that are depicted on the 1538Z SAR image.

Table 4.2 summarizes all input parameter values used for this Hi-Res 2 case study. Note that Re is calculated from (2.28) instead of being chosen directly, and that the Coriolis parameter f equals zero because we expect the BLCE solutions to have time scales on the order of an hour or less (Lambert 1995). Additionally, we specify only one wavenumber in each of the x- and y-directions in the model, enabling us to set $l = 1$ and $m = 1$ in (2.43) - (2.46).

After initializing the model, we integrate until we attain a state of quasi-equilibration. We observe this readily by plotting the dimensionless energy ($y^T Ay$) of the time-dependent amplitude coefficients, which follows from (2.55).

DETERMINATION OF THE
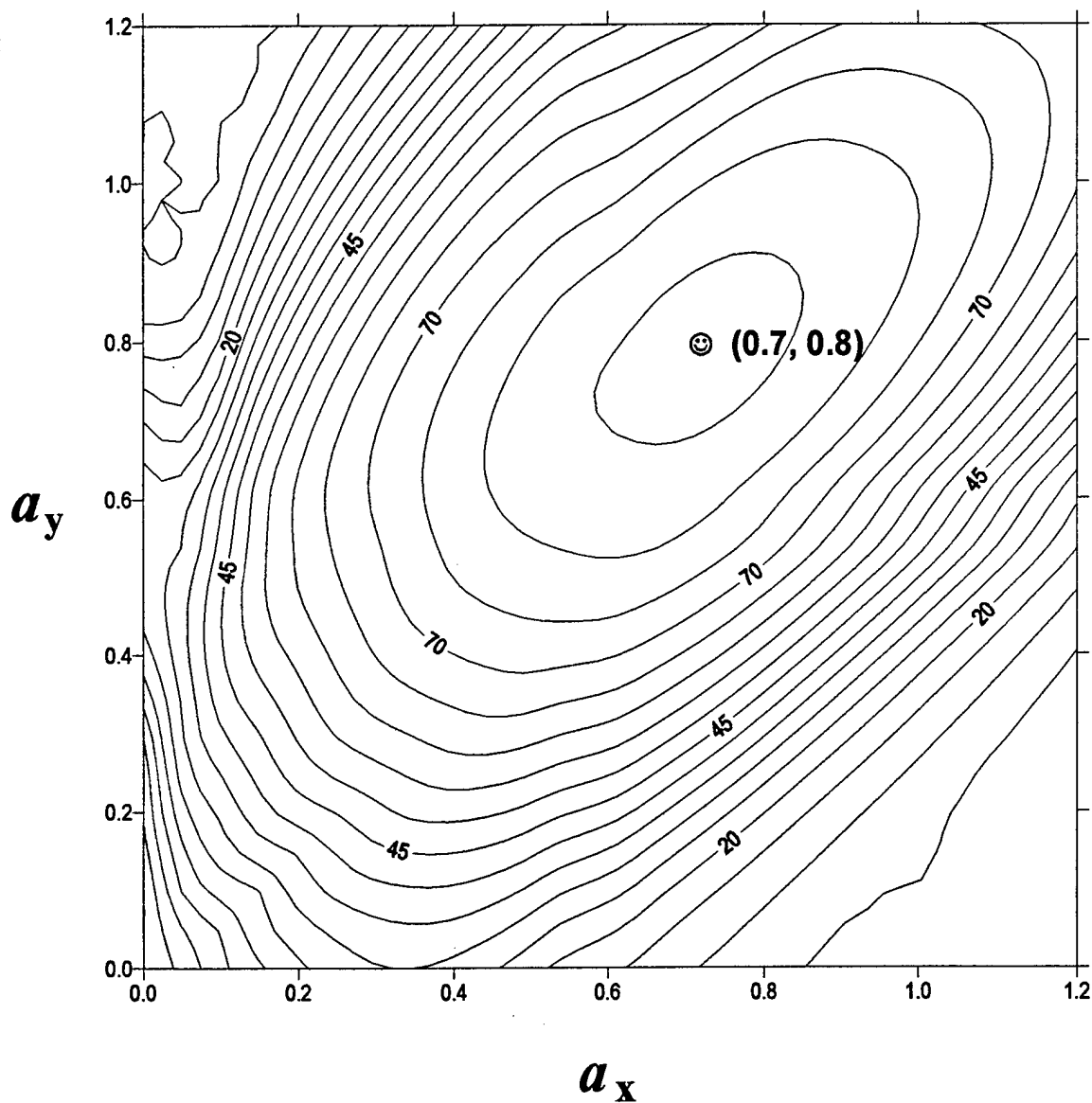# PREFERRED ASPECT RATIO

Figure 4.2. Contour plot of the real part of the 50th eigenvalue from the linear stability analysis from
Sonde 1 data. The maximum dimensionless growth rate indicates the preferred aspect ratios
(0.7, 0.8). The associated model parameter values are given in Table 4.2.

PARAMETER	VALUE
HEIGHT OF TOP OF DOMAIN (z_T)	609 m
HEIGHT OF BOTTOM OF DOMAIN (h_{LB})	10 m
HEIGHT OF INVERSION (z_i)	409 m
HEIGHT OF SURFACE LAYER (z_{SL})	20 m
ASPECT RATIO IN THE X-DIRECTION $\left(a_x\right)$	0.7
ASPECT RATIO IN THE Y-DIRECTION $\left(a_y\right)$	0.8
REYNOLDS NUMBER (Re)	359.4
MEAN WIND SPEED / DIRECTION AT $z = z_T$	6.0 ms^{-1} / 300^0
MEAN WIND SPEED / DIRECTION AT $z = h_{LB}$	0.93 ms^{-1} / 319^0
U MEAN WIND PROFILE PARAMETER (d_U)	2.5
V MEAN WIND PROFILE PARAMETER (d_V)	-3.0
ACCELERATION OF GRAVITY (g)	9.8 ms^{-2}
CORIOLIS PARAMETER (f)	0 s^{-1}
EDDY VISCOSITY $\left(v\right)$	1 m^2s^{-1}
EDDY CONDUCTIVITY $\left(\kappa\right)$	10 m^2s^{-1}
PRANDTL NUMBER (P)	0.1
SEA SURFACE TEMPERATURE (T_{00})	27.8 ^0C
TEMPERATURE AT $z = h_{LB}$ (T_{10})	24.9 ^0C
MIXING RATIO AT SEA SURFACE	22.3 $g\ kg^{-1}$
MIXING RATIO AT $z = h_{LB}$	13.6 $g\ kg^{-1}$
RAYLEIGH NUMBER (Ra)	-1
SCHRAMM VELOCITY CONSTANT (s_m)	0.67
SCHRAMM THERMAL CONSTANT (s_T)	1.95

As noted in Section 3.1, we empirically chose the value of the numerical nonlinear dissipation coefficient d to be 0.1; it remains fixed--as do the parameters in Table 4.2--for the two Sonde 1 cases presented here. What we do alter, however, is the value of the scale factor s_f from (3.7), which was initially implemented to expedite the integration process in a way that has absolutely no impact on the linear analysis, nor in principle, on the nonlinear advection terms. However, changing the value of s_f (and nothing else) does alter the weight of the nonlinear dissipation in the integration to yield rather interesting results. Table 4.3 shows the two Sonde 1 cases that we integrated with the scale factor and run time shown.

Table 4.3. Two Sonde 1 cases determined by scale factor value.

Case	d	s_f	Length of Integration
1	0.1	10^{-3}	175,000 s
2	0.1	10^{-2}	150,000 s

We arrived at these values after experimenting with d values in the range of 0 to 10, and s_f values in the range of 10^{-4} to 1. For the case with no dissipation ($d = 0$, $s_f = 1$), the dimensionless energy began to blow up at 175,000 s; in contrast, cases with strong numerical dissipation displayed extremely long, periodic oscillations with no sign of quasi-equilibration within reasonable periods of time. For each order of magnitude decrease in s_f (e.g., 1 to 10^{-1}), we realized an approximate 10 percent decrease in integration time. The selections of d and s_f values shown in Table 4.3 represent what we found to be the best combinations for speed and run quality.

The dimensionless energy is plotted for Case 1 and Case 2 in Figures 4.3 and 4.4, respectively. Case 2 reaches a state of quasi-equilibration around the dimensionless energy value 7.4×10^{10}, and so we stopped the run at 150,000 s (approximately 42 hours).

DIMENSIONLESS ENERGY
(CASE 1)
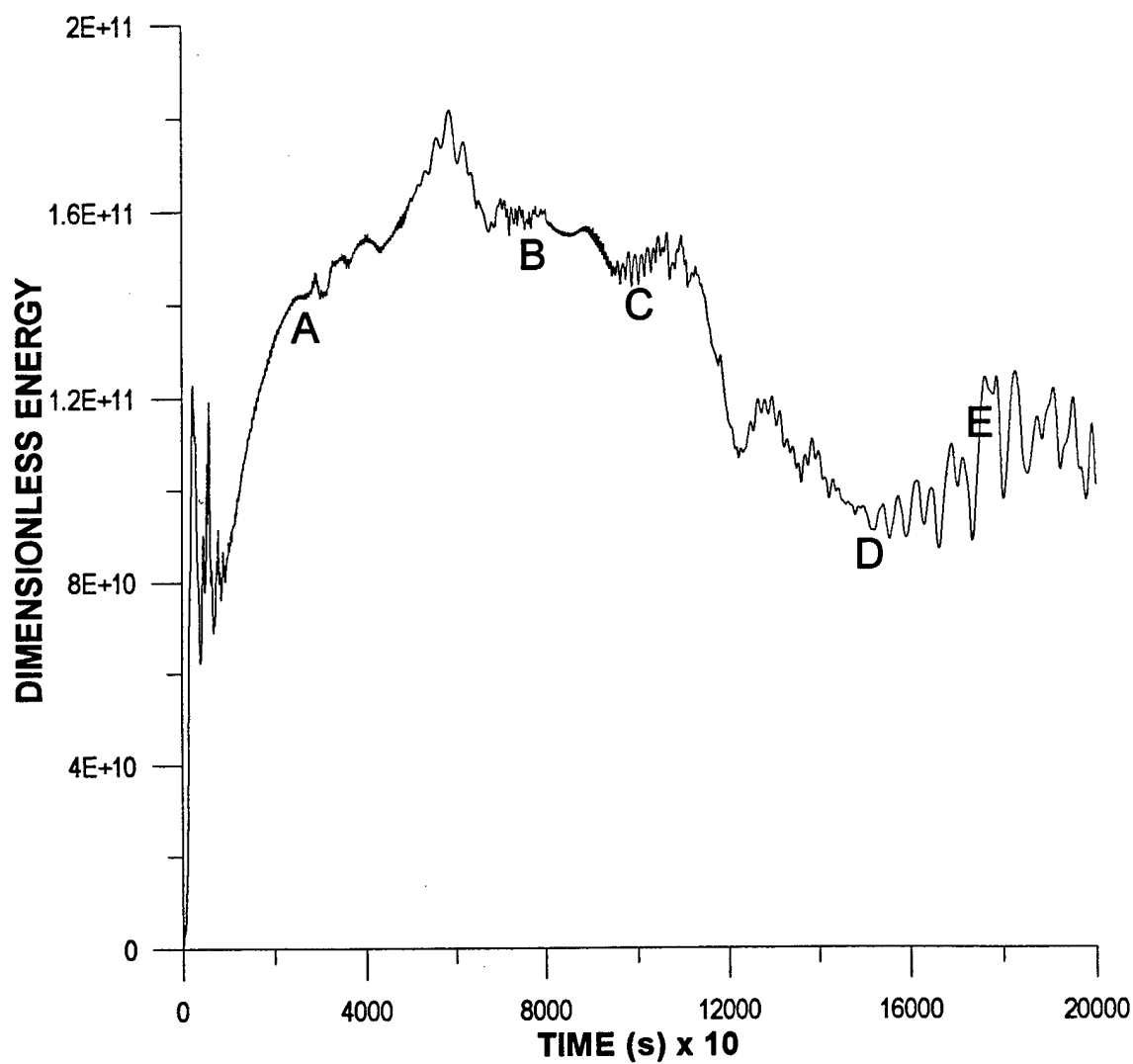

Figure 4.3. Case 1 time series plot of the dimensionless energy for the 50 time-dependent amplitude
coefficients. The system is quasi-equilibrated.
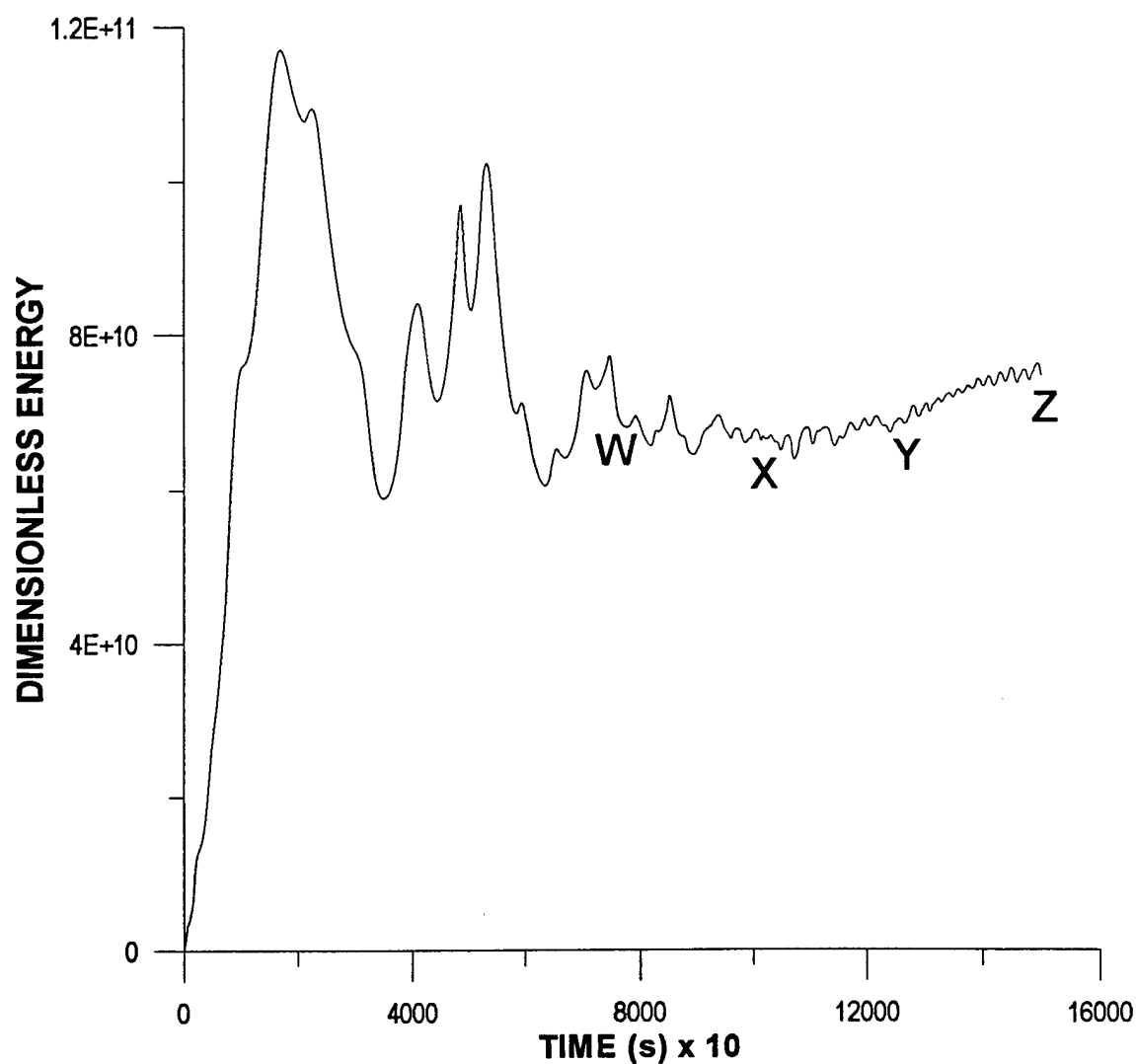
DIMENSIONLESS ENERGY
(CASE 2)

Figure 4.4. Case 2 time series plot of the dimensionless energy for the 50 time-dependent amplitude coefficients. The system is quasi-equilibrated.

In contrast, Case 1 appears to be settling near a value of 9.6×10^{10} by 150,000 s. Although the oscillation amplitude increases in magnitude between 150,000 s and 175,000 s, the mean energy is still less than 1.0×10^{11}. We integrate Case 1 further to 200,000 s to confirm that the oscillations do not continue to intensify without bound, and as Figure 4.3 shows, they apparently do not. They initially increase in magnitude, then decrease, with oscillations centered about 1.1×10^{11}. We choose 175,000 s as the case study termination point, however, because the model solution appears to stabilize by then, with minimal transient activity. Time series plots of the potential temperature amplitude coefficients θ_{11} for each case (Figure 4.5 for Case 1; Figure 4.6 for Case 2) show regular periodic oscillations, indicating that our choices for run termination times are appropriate. Note that Case 1 and Case 2 have dominant solution periods of 15 minutes and 67 minutes, respectively, which are consistent with the findings of Shirer (1986), Pyle (1987), and Haack and Shirer (1992) for BLCE.

Because the ultimate goal of this project is to study the impact that MABL secondary circulations have on the sea surface stress patterns as observed by SAR, we calculate the stress at the lower boundary of the model domain using the following equation:

$$\tau_r = C_d \rho_0 \left[(U_{h_{LB}} + u_r)^2 + (V_{h_{LB}} + v_r^{\,2}) \right]. \qquad (4.1)$$

Here, $U_{h_{LB}}$ and $V_{h_{LB}}$ are the horizontal components of the mean background wind at the lower boundary; u_r and v_r are the horizontal components of the wind due to the roll or cell at the lower boundary h_{LB}; ρ_0 is the density from (2.2) with a typical value of 1 kg/m^3; and C_d is the coefficient of drag, with a typical value of 1/900 (Stull 1988). The computational output (CO) subroutine of the model also calculates the stress induced strictly by u_r and v_r to display the contribution from the rolls or cells independent of the mean wind contribution. For the stress plots presented in this study, we chose to include
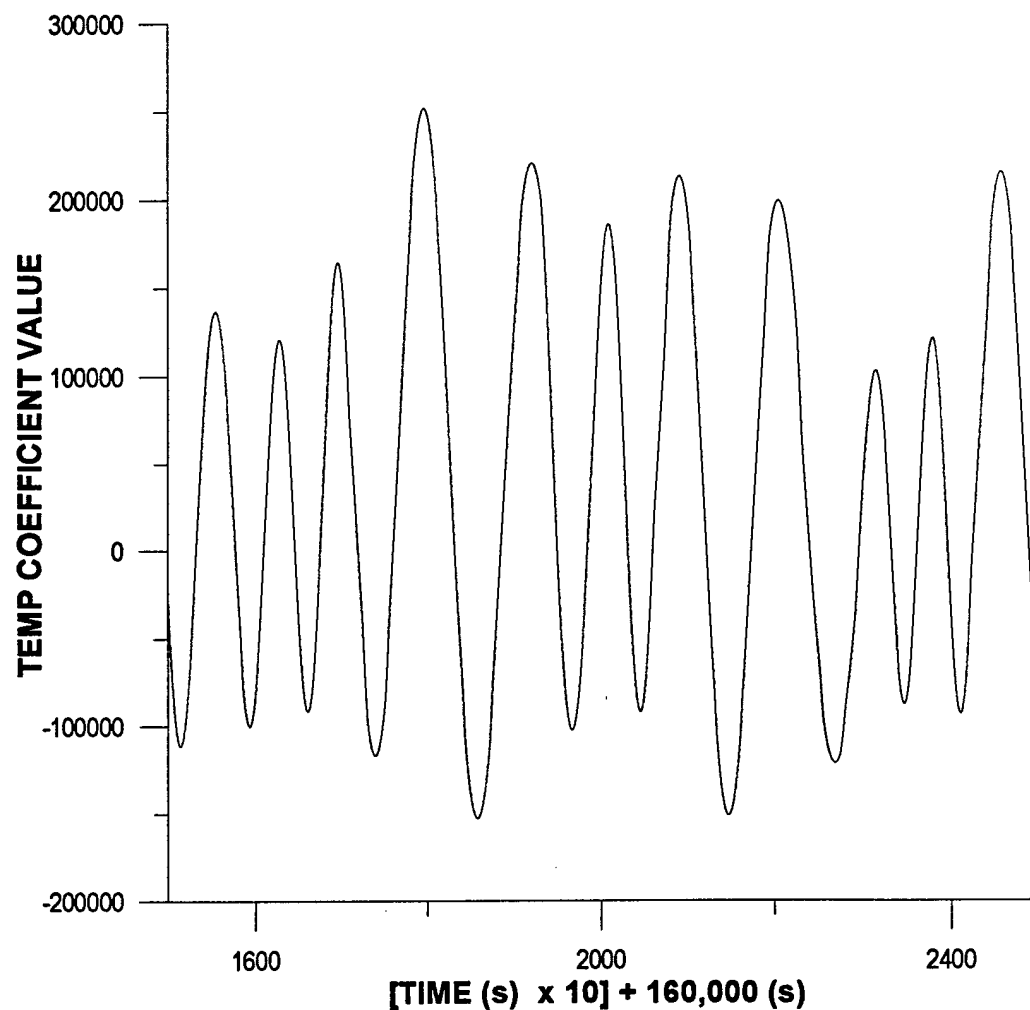
POTENTIAL TEMPERATURE AMPLITUDE
COEFFICIENT (CASE 1)

Figure 4.5. Time series (last 15,000 s) of one of the time-dependent potential temperature amplitude coefficients (θ_{11}) for Case 1, demonstrating that the solution has a dominant period of approximately 15 minutes.

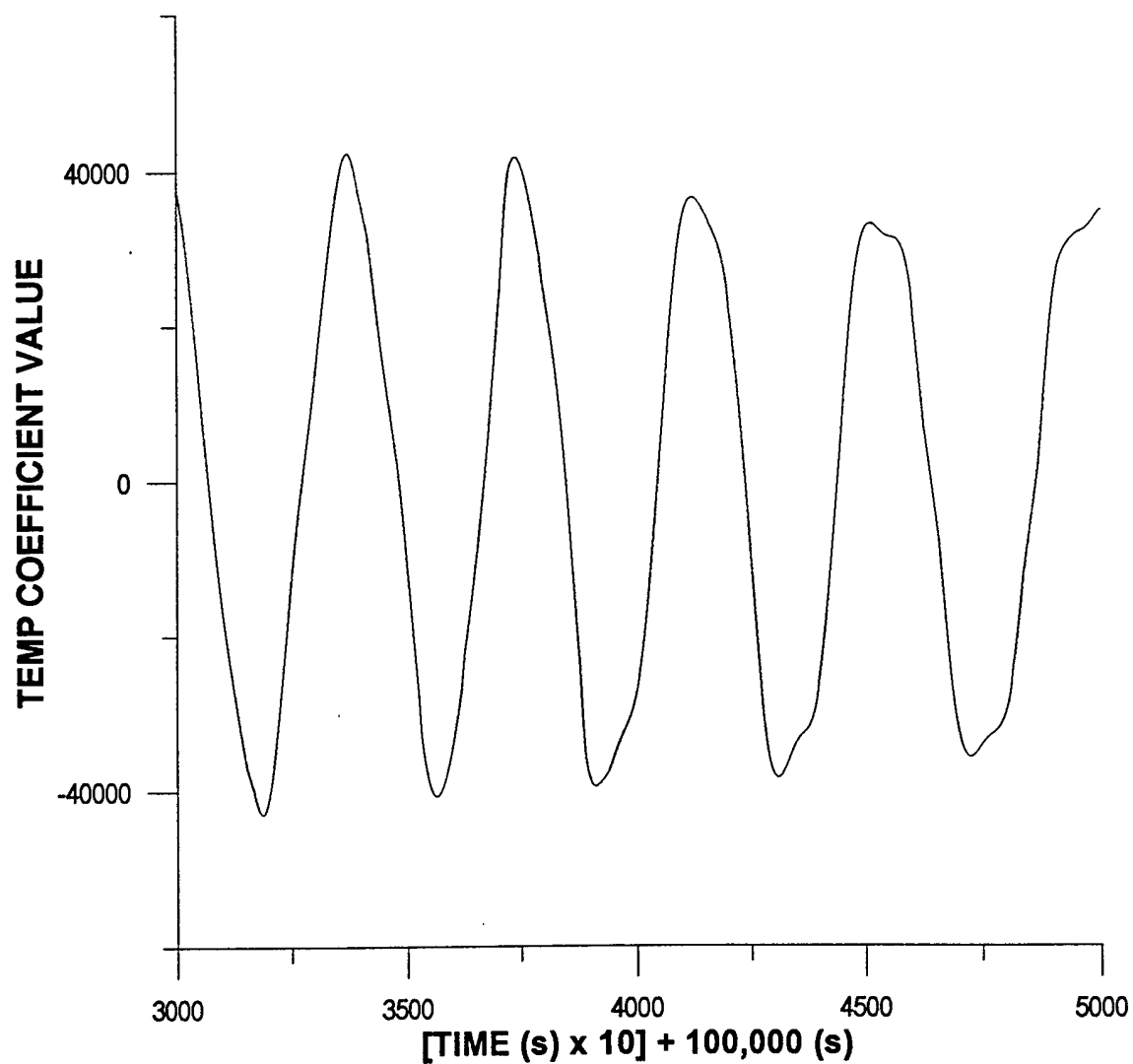# POTENTIAL TEMPERATURE AMPLITUDE COEFFICIENT (CASE 2)

Figure 4.6. Time series (last 20,000 s) of one of the time-dependent potential temperature amplitude coefficients (θ_{11}) for Case 2, demonstrating that the solution has a dominant period of approximately 67 minutes.

the contribution of the background wind, as that would apply better to the atmospheric case.

A salient application of stress planviews is the determination of the structural type of BLCE regime under investigation, whether quasi-two-dimensional with rolls, fully three-dimensional with cells, or somewhere in between. While we are primarily concerned with the regime of the final stabilized solution for each case, we are also interested in observing the pattern evolution between regimes. To do so, we occasionally extract data during the course of the integrations and pass it through the CO subroutine. On the dimensionless energy time series plots (Figures 4.3 and 4.4), we have identified the points at which data were extracted--A through E for Case 1, and W through Z for Case 2--and we have summarized the results in Table 4.4. As we illustrate below, note that in Case 1 the model

Table 4.4. Summary of structure types at the points depicted on the energy plots (Figures 4.3 and 4.4) for Case 1 and Case 2. The type is determined from the surface stress patterns.

CASE	TIME STEP (s)	POINT	STRUCTURE	ENERGY LEVEL
1	25,000	A	Rolls	1.41×10^{11}
1	75,000	B	Transition	1.59×10^{11}
1	100,000	C	Cells	1.48×10^{11}
1	150,000	D	Cells	9.58×10^{10}
1	175,000	E	Cells	1.11×10^{11}
2	75,000	W	Rolls	7.65×10^{10}
2	100,000	X	Rolls	6.75×10^{10}
2	125,000	Y	Rolls	6.86×10^{10}
2	150,000	Z	Rolls	7.44×10^{10}

solution starts as quasi-two-dimensional, passes through a transitional phase and then becomes fully three-dimensional. Case 2, in contrast, is strictly quasi-two-dimensional throughout the length of the integration, with no indications of changing. Remarkably, both cases were run from the same initial conditions. Because the magnitude of the

dimensionless energy is much greater overall in Case 1, we speculate that the *transition* from quasi-two-dimensional to three-dimensional patterns requires higher levels of energy—energy that is reduced in Case 2 by using a larger value of s_f, which serves to strengthen the nonlinear dissipation. A majority of the preliminary runs we performed produced energy signatures like that depicted in Case 1 and yielded three-dimensional solutions after quasi-equilibration had occurred. We therefore postulate that higher energy levels are a necessary (but not sufficient) condition for a regime to transition from a quasi-two- to three-dimensional pattern. Owing to time limitations, we were unable to explore this hypothesis further but suggest that future studies address it.

The plot of stress magnitudes at the lower boundary for Case 1 (at Point E, Figure 4.3) is shown in Figure 4.7. Higher stress regions are depicted by lighter shading to match the brightness of the high-stress regions on a SAR image, and we are gratified that the magnitudes of the dimensional stress, with orders of magnitude of 10^{-2} Nm^{-2}, are consistent with those found by Alpers and Brümmer (1994) (although their 10 m winds were more intense). As previously noted, the Case 1 stress pattern clearly exhibits a fully three-dimensional flow field whose structure is oriented nearly perpendicular to the direction of the mean background wind at the lower boundary. We contrast this result with that in Figure 4.8, which shows the surface stress for Case 1 at 100,000 s (Point C, Figure 4.3). Here the orientation is aligned 14^0 to the right of the background wind, which is well within the range of typically observed values of -20^0 to $+30^0$ (Etling and Brown 1993). This orientation also more closely matches the pattern depicted by the 1538Z SAR image shown in Sikora *et al.* (1995) as well as Lambert's (1995) findings. From a modeling standpoint, discovering that cells can become oriented normal to the background wind is a success; this is the first case in which we observed such behavior, assuring us that the orientation is not locked to the direction of the mean wind as a result of a modeling assumption. From a meteorological perspective, however, we felt initial disappointment because we had not captured the same cell orientation as the SAR image
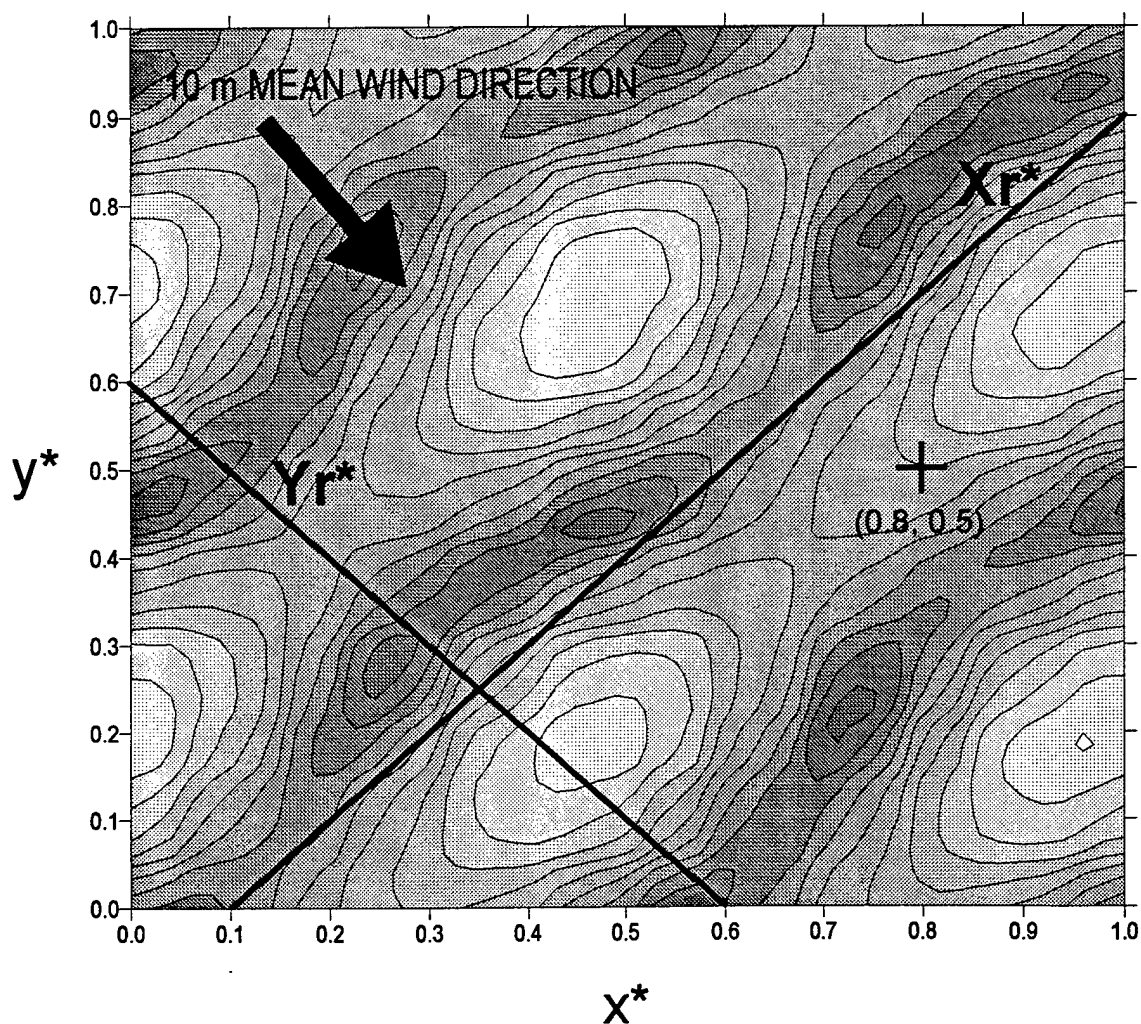
STRESS AT LOWER BOUNDARY
(CASE 1, POINT E)

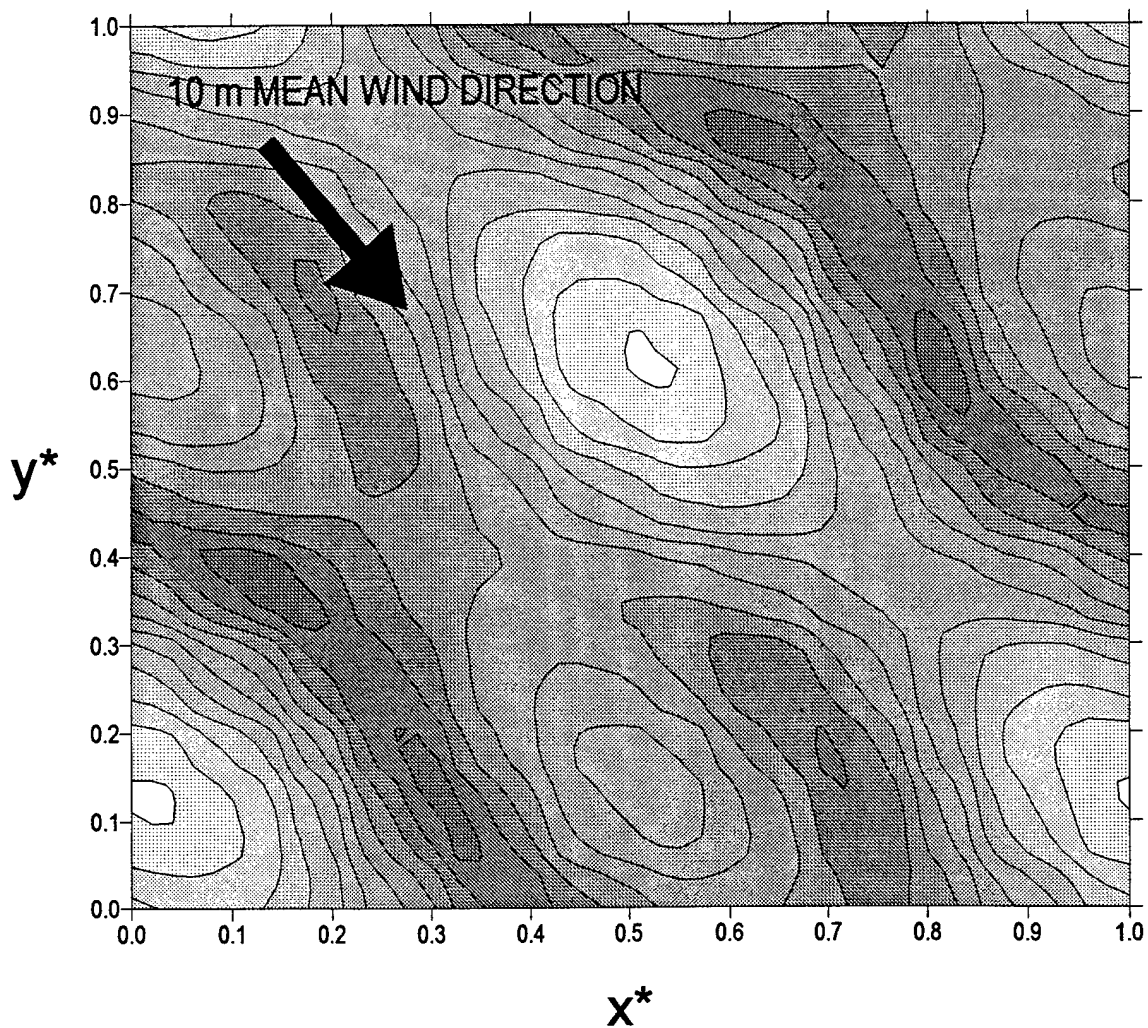Figure 4.7. Planview of stress magnitudes at $z* = 0$ imposed by the background wind and secondary circulations (cells), as predicted in Figure 4.1. Consistent with SAR imagery, regions of higher stress are shaded lightly and regions of lower stress are shaded heavily. The domain shape $(x*/y*)$ is chosen to agree with the ratio $a_y/a_x = 1.15$, and Xr* and Yr* represent the rotated cell coordinate system. The along-mean wind axis Xr* is perpendicular to the cross-mean axis Yr* but does not appear as such due to the domain shape $(x*/y*)$ scaling. The contour interval is 5×10^{-4} Nm^{-2}, and the + sign denotes the point at which profiles are calculated.

STRESS AT LOWER BOUNDARY
(CASE 1, POINT C)

Figure 4.8. Planview of stress magnitudes at $z* = 0$ imposed by the background wind and secondary circulations (cells), as predicted by Figure 4.1. Consistent with SAR imagery, regions of high stress are shaded lightly and regions of lower stress are shaded heavily. The domain shape (x^*/y^*) is chosen to agree with the ratio $a_y/a_x = 1.15$, and the contour interval is the same as that used in Figure 4.7.

at the same time that model transients had settled down. However, a SAR image records an instant in time, not an evolution, and it is quite possible that a change occurred in the orientation of the sea surface stress pattern after the 1538Z SAR image was taken. Of course we cannot prove such an assertion here, but we note that having the secondary circulation aligned normal to the direction of the mean wind is not without precedent for an inflection point mode BLCE (e.g., Brown 1980). Later, we will show that the Case 2 modified (post-cell) wind speed profile contains two points of inflection, consistent with our findings here.

In this study, we do not focus on the transition from quasi-two- to three-dimensional regimes; however, we include in Figure 4.9 the stress pattern plot for Point B of Figure 4.3, which illustrates the transitional phase stress pattern for Case 1. Note that while the quasi-two-dimensional roll structure is still quite prominent, there is evidence of cellular activity.

The stress pattern for Case 2 (Point Z, Figure 4.4) is depicted in Figure 4.10 and is quasi-two-dimensional, indicating that rolls are dominant in the model solution. There is a hint of three-dimensionality in the stress pattern (small cellular structures along the diagonal), but it is negligible; the phenomenon may be due to limitations of the contouring software in handling the very small variations along the SE-NW diagonal, or simply that the gridding used was too coarse. The rolls for this case are closely aligned with the direction of the mean background wind and remain fixed in orientation throughout the length of the run, indicating a more robust model solution. Based upon the extensive work done by Woodcock (1940, 1975) and Deardorff (1976), we recall from Figure 4.1 that the atmospheric parameter values used (Table 4.1) should yield a three-dimensional cellular solution. Accordingly, we attribute the quasi-two-dimensionality observed in Case 2 strictly to numerics--the larger s_f value simply altered dissipation sufficiently to cause the model solution to seek a different, lower energy attractor, a quasi-two-dimensional one.
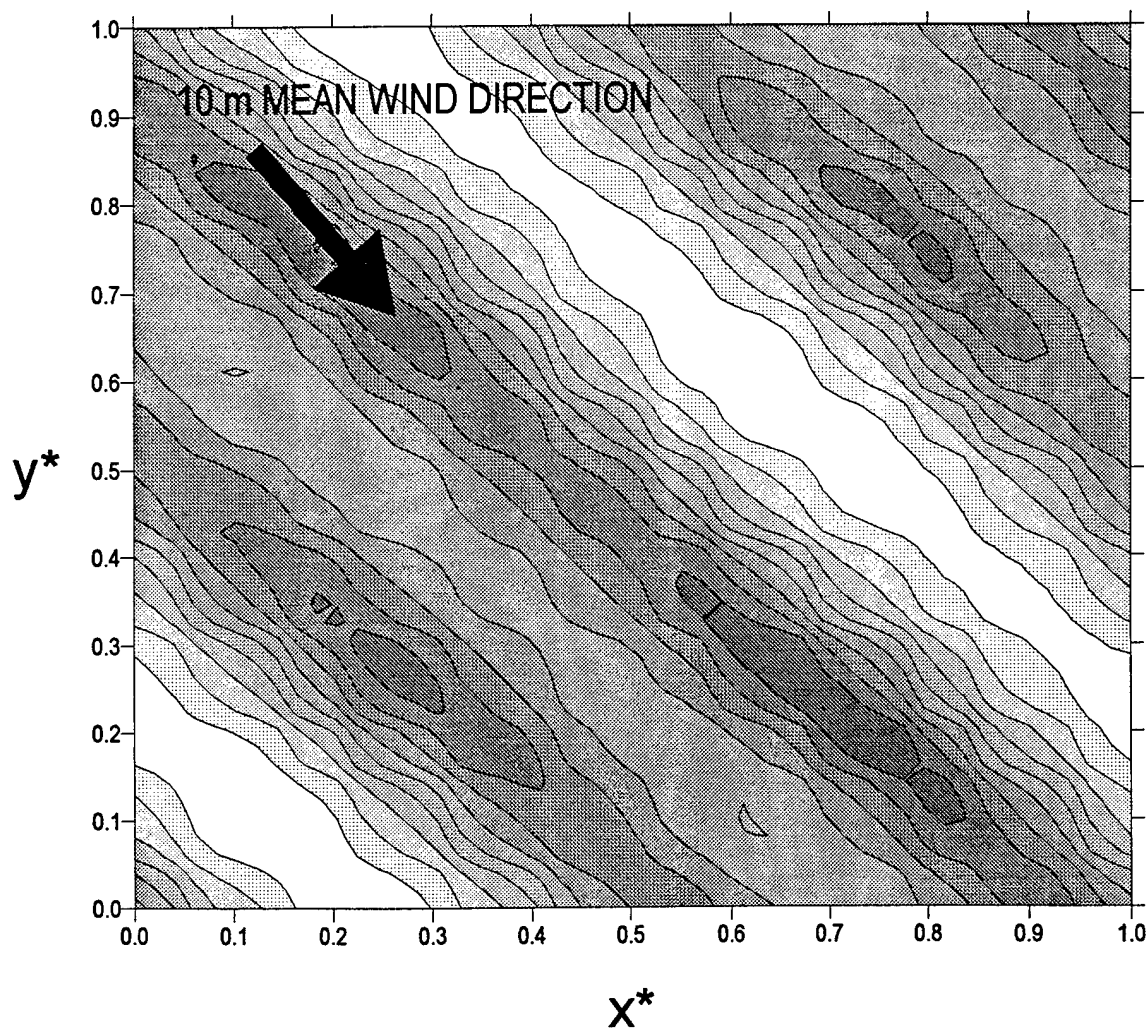
STRESS AT LOWER BOUNDARY
(CASE 1, POINT B)

Figure 4.9. Planview of stress magnitudes at $z* = 0$ imposed by the background wind and secondary circulations in transition between rolls and cells. Consistent with SAR imagery, regions of high stress are shaded lightly and regions of lower stress are shaded heavily. The domain shape $(x*/y*)$ is chosen to agree with the ratio $a_y/a_x = 1.15$, and the contour interval is the same as that used in Figure 4.7.

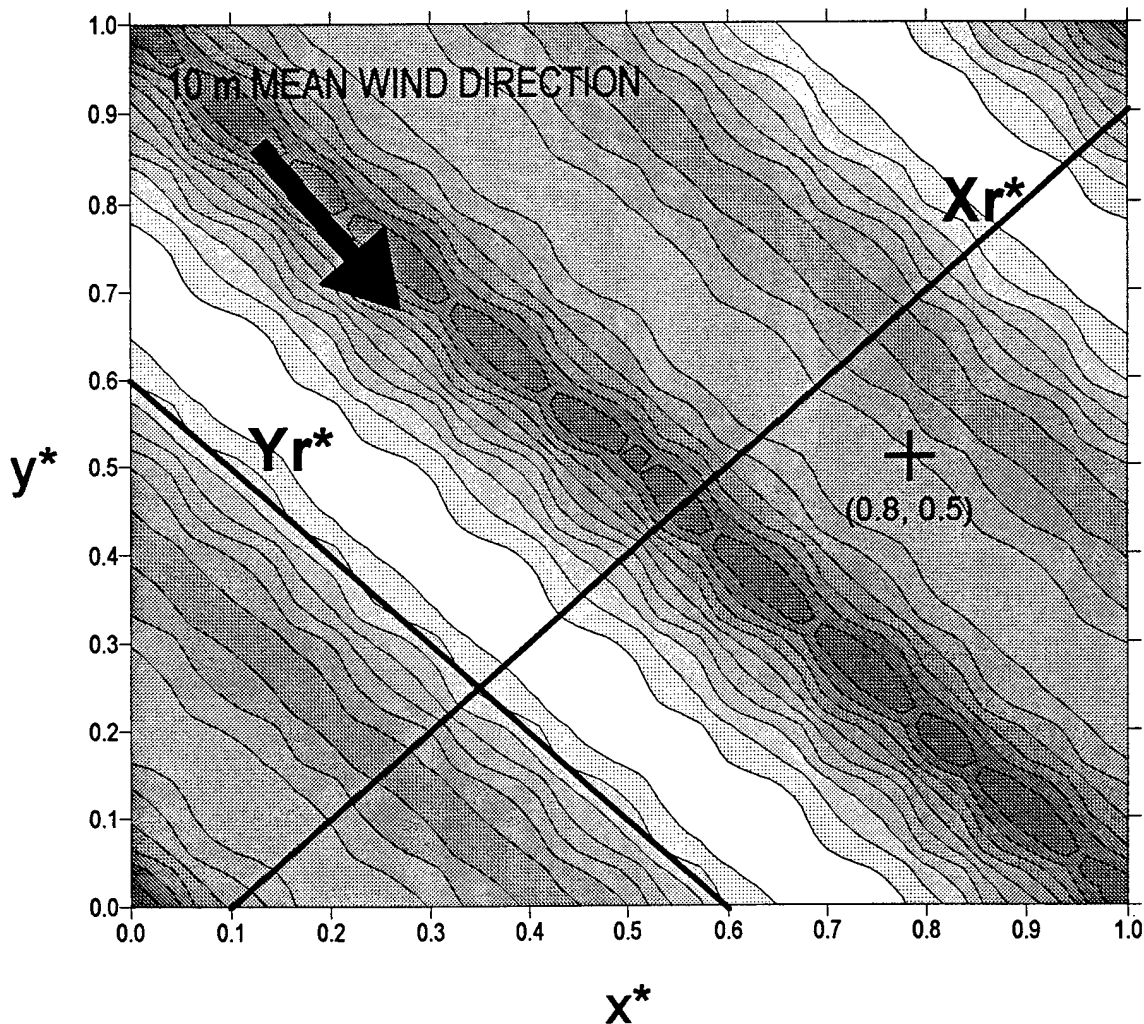# STRESS AT LOWER BOUNDARY
(CASE 2, POINT Z)

Figure 4.10. Planview of stress magnitudes at $z^* = 0$ imposed by the background wind and secondary circulations (rolls). Consistent with SAR imagery, regions of high stress are shaded lightly and regions of lower stress are shaded heavily. The domain shape (x^*/y^*) is chosen to agree with the ratio $a_y/a_x = 1.15$, and Xr* and Yr* represent the rotated roll coordinate system as in Figure 4.7. The contour interval is also the same as that used in Figure 4.7, and the + sign denotes the point at which profiles are calculated.

We therefore postulate that Case 1 is more physically plausible than Case 2 with the atmospheric input variables used. Nevertheless, we will compare and contrast both cases to further evaluate model capabilities and limitations.

Because the cellular structures in Case 1 are aligned nearly normal to the direction of the background mean wind (Figure 4.7) and because the rolls in Case 2 are nearly parallel to the mean wind, we expect the dominant solution period to be smaller for Case 1. Agreeably, it is, as we determined from the time series plots for θ_{11} (Figures 4.5 and 4.6); the Case 1 period is 15 minutes while the Case 2 period is 67 minutes.

On Figures 4.7 and 4.9 we have drawn new, rotated axes, Xr^* and Yr^*, along which we take cross sections of the domain to contour values of the streamfunctions, vertical velocity and potential temperature. These rotated axes are determined differently from the $\tilde{x}^*$ and $\tilde{y}^*$ axes used in Lambert (1995). Here, Xr^* and Yr^* represent the cross- and along-mean wind axes, and they are perpendicular to one another. On the stress planviews, however, they do not appear as such due to domain shape scaling. The rotated axes are given by

$$Xr^* = x^* - y^* \tag{4.2}$$

$$Yr^* = x^* + y^*, \tag{4.3}$$

and the rotated streamfunctions are specified by

$$\psi_r^* = \psi^* + \eta^* \tag{4.4}$$

$$\eta_r^* = \psi^* - \eta^*. \tag{4.5}$$

Note that we only illustrate physically relevant streamfunction components in our cross sections; that is, η^* is contoured only along the Xr^* axis as η_r^*, and ψ^* is contoured only along the Yr^* axis as ψ_r^*. For Case 1, Xr^* runs along the orientation of the cells and Yr^* runs across the cells. For Case 2, Xr^* and Yr^* are the cross- and along-roll axes, respectively.

We begin by contouring values of the streamfunctions for both cases (Figures 4.11 and 4.12) to ensure dimensional consistency with the stress plots and to determine the vertical extent of the secondary circulations. A cursory glance at the flows shown for Case 1 (Figure 4.11) clearly suggests a fully three-dimensional structure because flows are evident in both cross sections--this is what we expected from Figure 4.7. Similarly, the quasi-two-dimensional structure displayed by the stress pattern in Figure 4.10 for Case 2 clearly coincides with the flows visualized in Figure 4.12, for there are only circulations present along the Xr^* axis, the cross-roll axis in this case. Overall, the circulations are stronger in Case 1 than in Case 2.

We had hoped that the addition of an inversion (at $z_i^* = 0.7$) would cap the circulations as it did for Laufersweiler and Shirer (1995). From Figures 4.11 and 4.12, we can see that it appears to be doing so for both cases, with only slight anomalies. For Case 1 (Figure 4.11), the along-Xr^* axis plot shows circulations capped almost perfectly by the inversion with very weak, and certainly acceptable, perturbations above the inversion base at $z^* = 0.7$. Along the Yr^* section, the circulations penetrate into the inversion, though the relative weakness of ψ_r^* above z_i^* is comforting. Given the relatively small inversion strength (1.8 ^{0}C/200m), this too seems physically acceptable. Similarly, the Case 2 flow shown along the Xr^* axis in Figure 4.12 is quite reasonable with a well-defined circulation below z_i^* and only negligible perturbations into the inversion. Overall, these cross sections are encouraging and illustrate that the model is capable of adequately capping weak to moderate flows with an inversion.
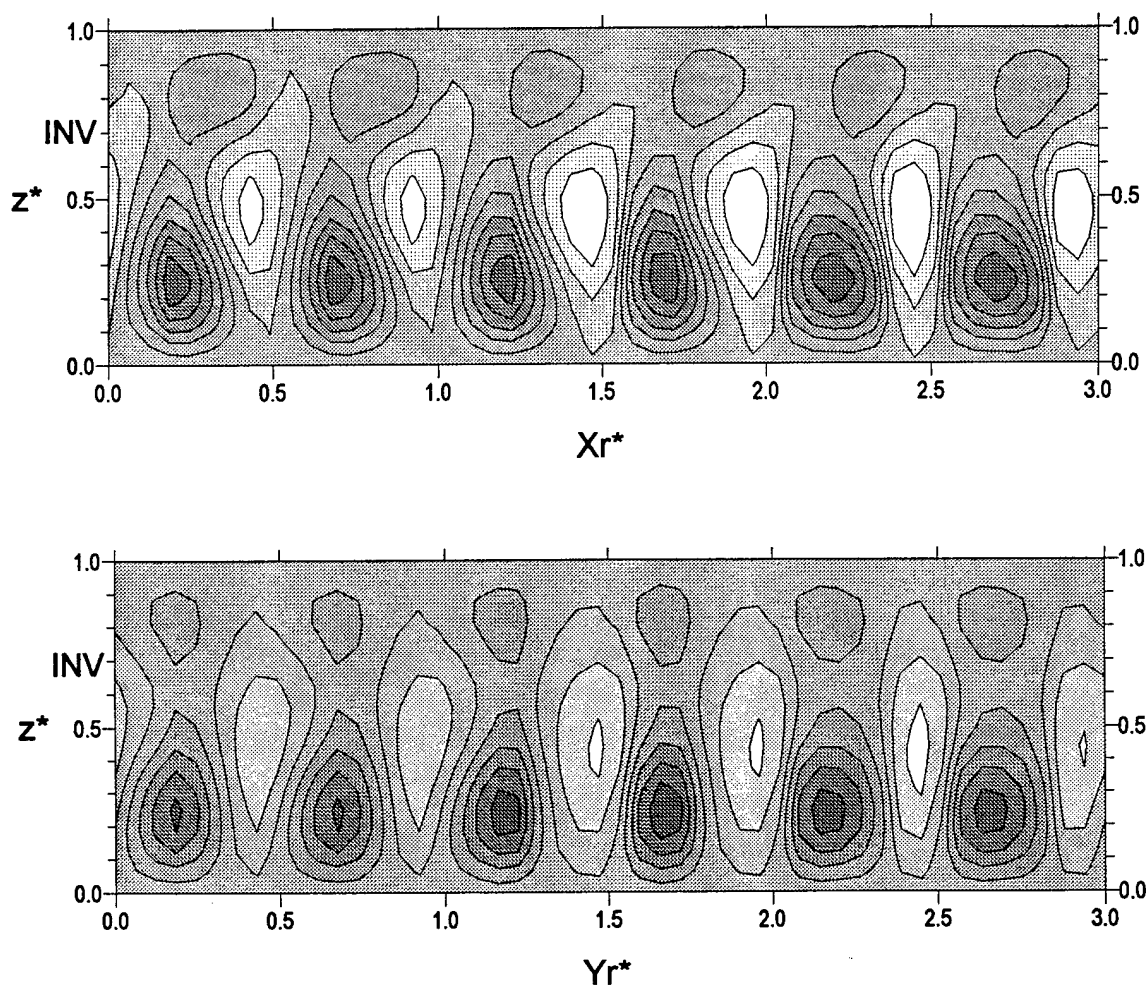
STREAMFUNCTION
CROSS SECTIONS
(CASE 1)

Figure 4.11. Cross sections of contoured streamfunctions using rotated horizontal axes from Figure 4.7:

(Top) η_r^* is contoured along the Xr^* axis, and (Bottom) ψ_r^* is contoured along the Yr^* axis.

Shaded regions represent negative values while lighter regions represent positive values. The contour interval is consistent in the top and bottom cross sections, as well as with Figure 4.12.
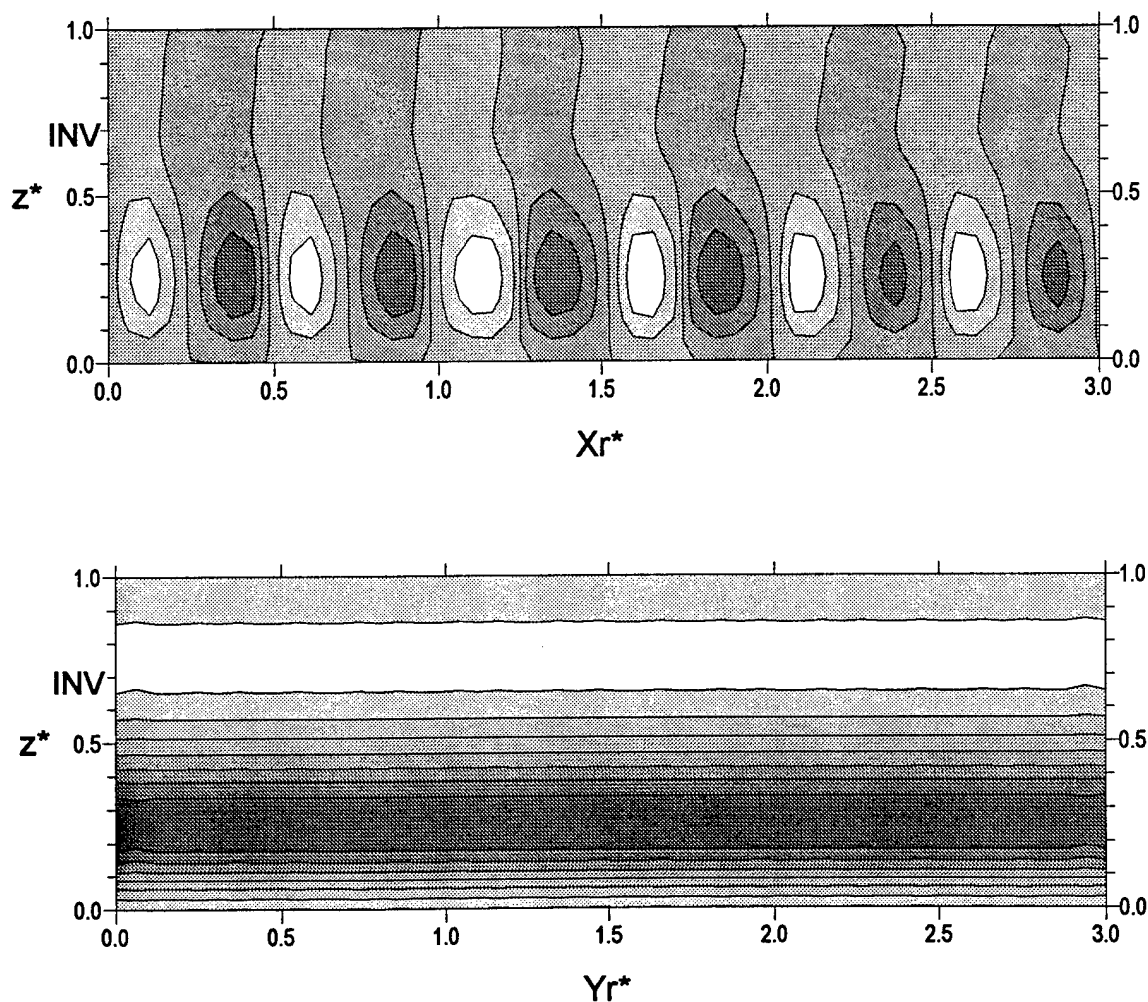
STREAMFUNCTION
CROSS SECTIONS
(CASE 2)

Figure 4.12. Cross sections of contoured streamfunctions using rotated horizontal axes from Figure 4.9:

(Top) η_r^* is contoured along the Xr^* axis, and (Bottom) ψ_r^* is contoured along the Yr^* axis.

Shaded regions represent negative values while lighter regions represent positive values. The contour interval is consistent in the top and bottom cross sections, as well as with Figure 4.11.

Figures 4.13 and 4.14 display cross sections of vertical velocities for Cases 1 and 2, respectively. One notable feature in both cases is the presence of vertical velocity maxima at approximately 0.3 of the depth of the boundary layer ($z^* \approx 0.2$), which is consistent with convective boundary layer observations (e.g., Lenschow *et al.* 1980) and other more complex model simulations (e.g., large eddy simulation [LES], Schmidt and Schümann [1989]). In the Yr^* cross section of Case 1 (Figure 4.13) and both cuts from Case 2 (Figure 4.14), the vertical velocity contours are contained below the base of the inversion at $z_i = 0.7$, with the exception of very minor perturbations. The Xr^* cross section of Case 1, however, appears as an anomaly with a wavenumber-three signature and the maximum updraft just below z_i. We attribute this pattern to the location of the Xr^* axis in Figure 4.7, which cuts through a complicated three-dimensional pattern between the high- and low-stress regions, and encounters a plethora of small-scale contour variations. Had we taken a different cross section, we would expect cleaner results. We are quite pleased with the Xr^* cross section of Case 2, for it clearly captures the observed phenomenon of narrow updrafts and broad downdrafts. We are somewhat perplexed by the Yr^* section of Case 2, however, since the existence of updrafts in this cross sections suggests a three-dimensional flow; yet all other indicators point to a quasi-two-dimensional regime. We defer speculation until the solution is visualized in three dimensions.

We turn now to vertical velocity profiles for a snapshot look at the variation of w with z^* at a fixed horizontal point ($x^* = 0.8$, $y^* = 0.5$), denoted on Figures 4.7 and 4.10. A Case 1 profile drawn in Figure 4.15 depicts a maximum updraft just above $z^* = 0.2$ (consistent with the cross section results), a downdraft just above $z^* = 0.5$ and a secondary, weaker updraft in the inversion layer. We believe the two former attributes accurately represent the physics of the boundary layer, while the latter attribute shows evidence of a very slight circulation within the inversion layer, consistent with the streamfunction and vertical velocity perturbations noted in Figures 4.11 and 4.13, respectively. The Case 2 vertical velocity profile is shown in Figure 4.16 and represents a nearly ideal profile, for there is
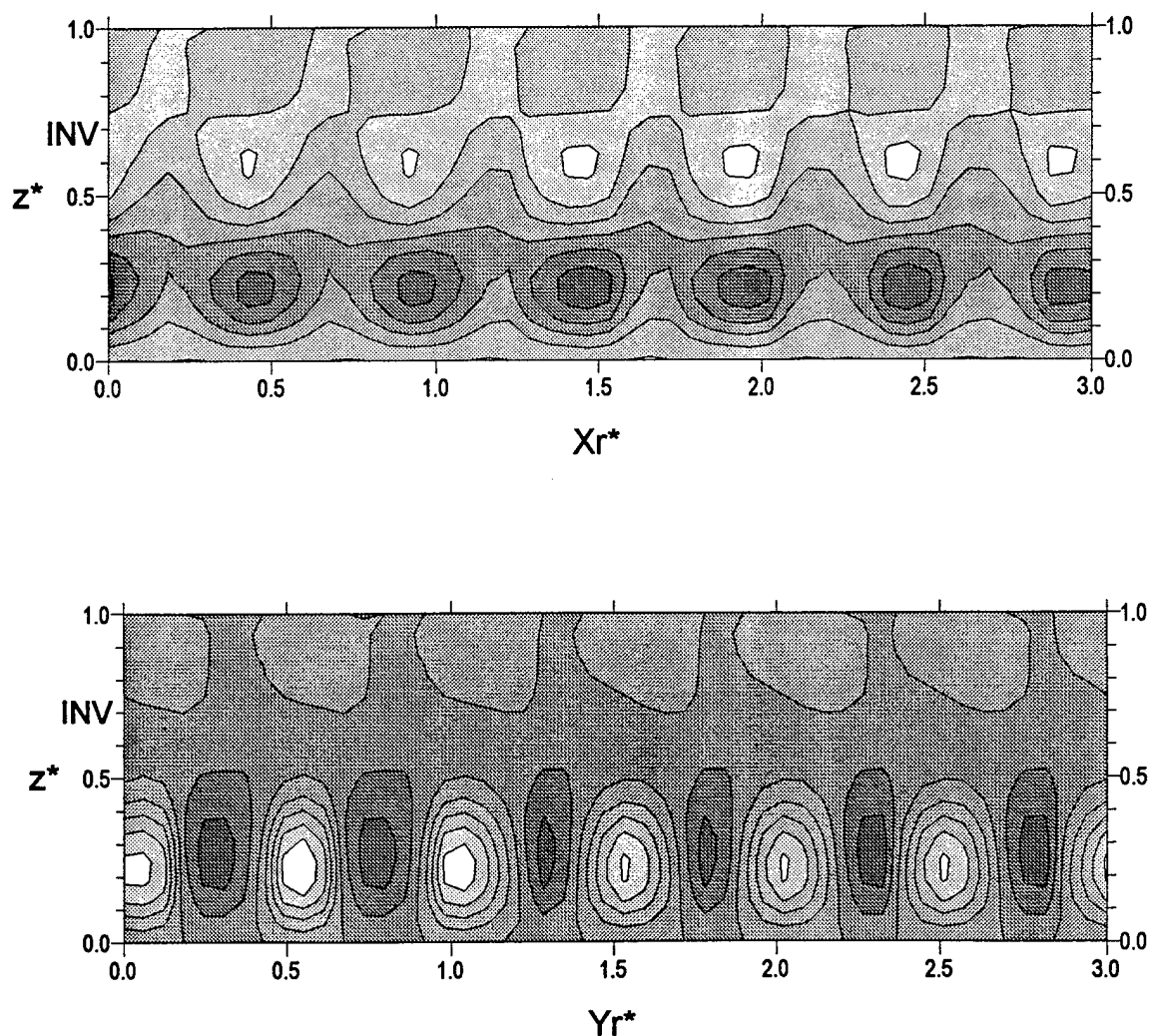
VERTICAL VELOCITY
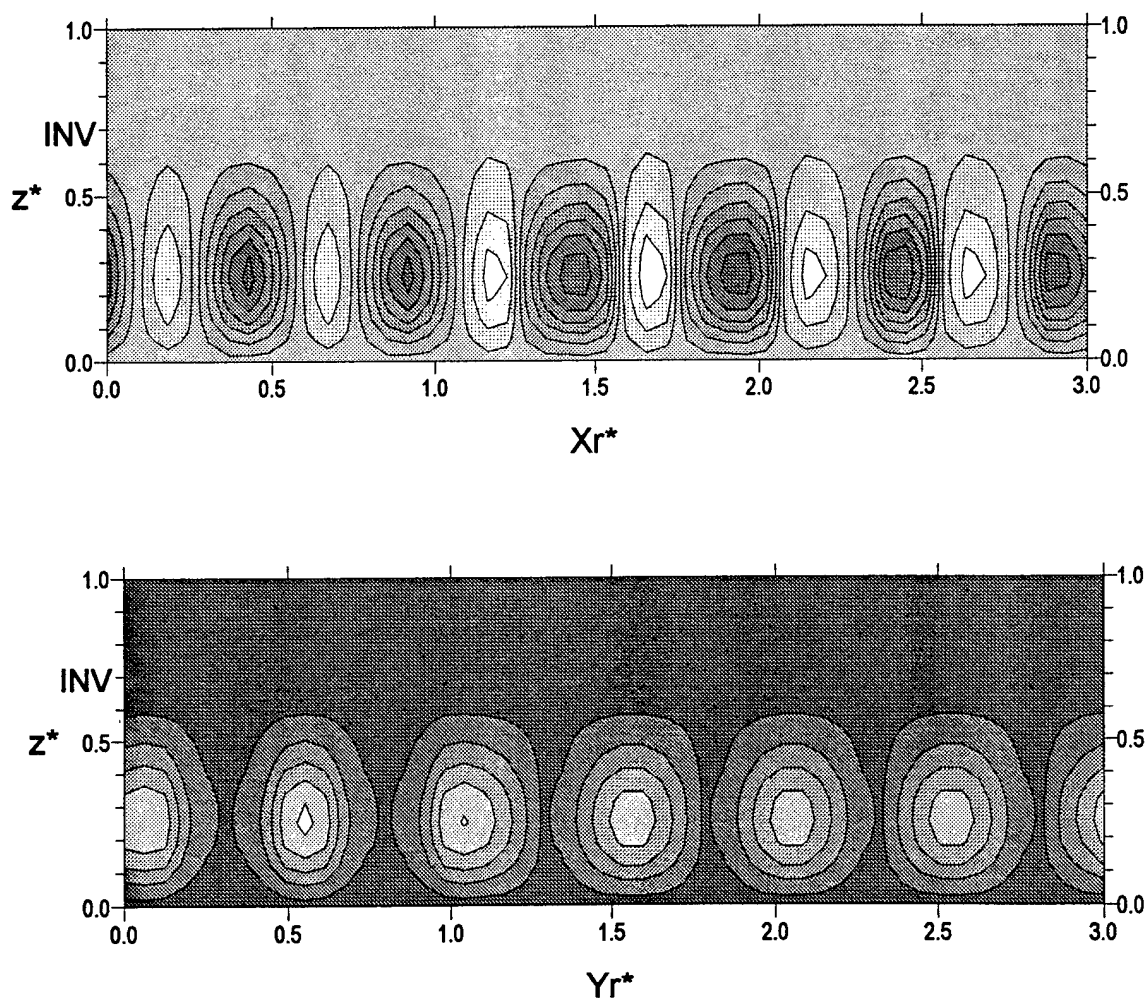# CROSS SECTIONS
(CASE 1)

Figure 4.13. Cross sections of contoured vertical velocity fields using rotated horizontal axes from Figure 4.7: (Top) w^* is contoured along the Xr^* axis, and (Bottom) w^* is contoured along the Yr^* axis. Shaded regions represent negative values (downdrafts) while lighter regions represent positive values (updrafts). The contour interval is consistent in the top and bottom cross sections, as well as with Figure 4.14.

VERTICAL VELOCITY
CROSS SECTIONS
(CASE 2)

Figure 4.14. Cross sections of contoured vertical velocity fields using rotated horizontal axes from Figure 4.9: (Top) w^* is contoured along the Xr^* axis, and (Bottom) w^* is contoured along the Yr^* axis. Shaded regions represent negative values (downdrafts) while lighter regions represent positive values (updrafts). The contour interval is consistent in the top and bottom cross sections, as well as with Figure 4.13.
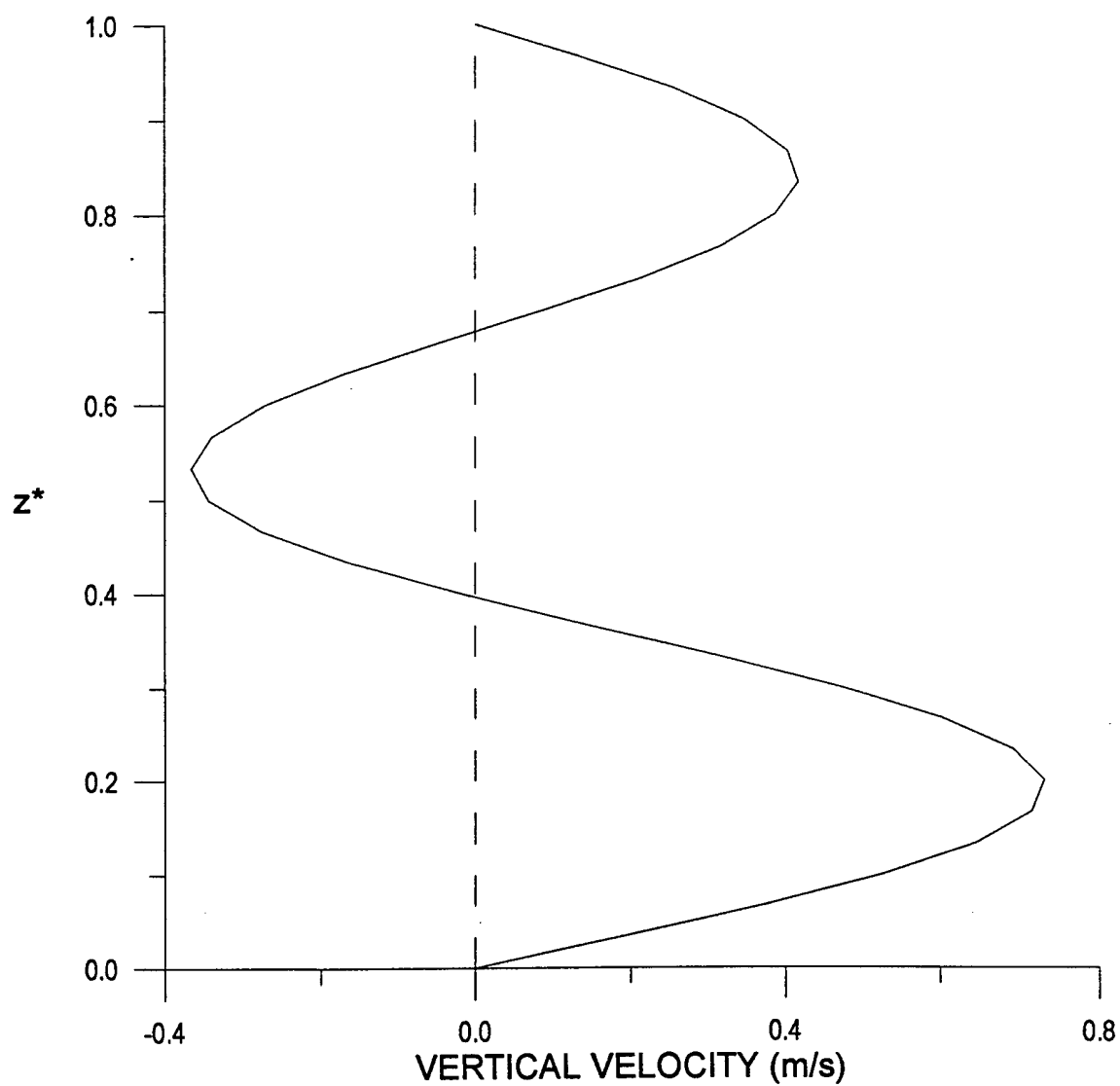
VERTICAL VELOCITY
(CASE 1)

Figure 4.15. Profile of the Case 1 vertical velocity (*m/s*) at (*x**, *y**) = (0.8, 0.5), denoted by + in Figure 4.7.
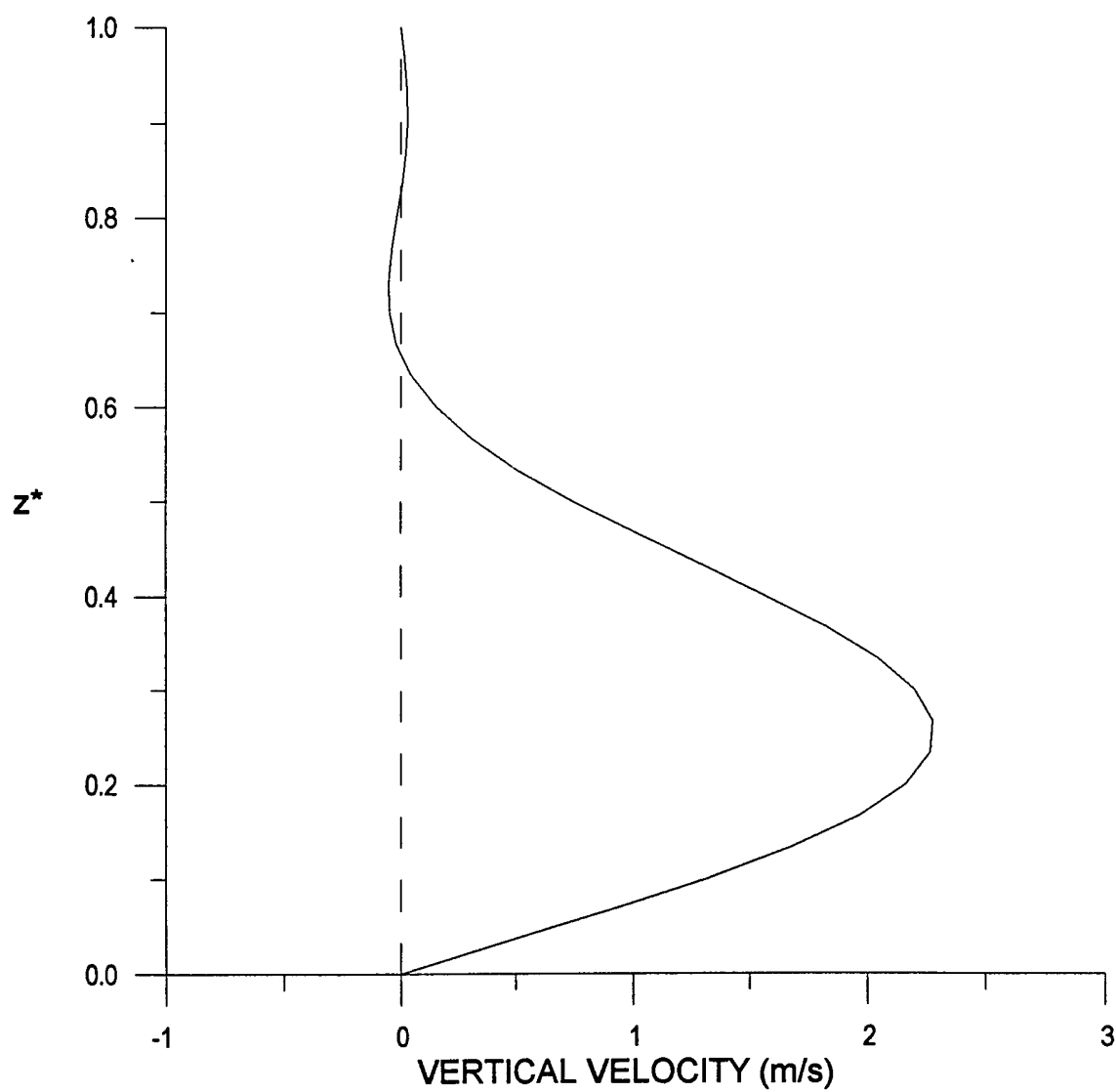
VERTICAL VELOCITY
(CASE 2)

Figure 4.16. Profile of the Case 2 vertical velocity (m/s) at (x^*, y^*) = (0.8, 0.5), denoted by + in Figure 4.10.

only one maximum in the vertical column at approximately 0.3 times the depth of the boundary layer. Additionally, w becomes negligible just below the base of the inversion and remains small throughout the inversion layer. We are also encouraged that the magnitudes of w found for both cases are acceptable for BLCE (Etling and Brown 1993).

We now examine the potential temperature perturbation cross sections shown in Figures 4.17 and 4.18 for Cases 1 and 2, respectively. A cursory glance reveals that the model has difficulty resolving temperature in these cross sectional views. However, there are three noteworthy phenomena captured by the model: 1) The region where the greatest temperature perturbations occur is *at the lower boundary*, indicating that our boundary conditions have captured the physics of a warm ocean below a cooler MABL, as Schmidt and Schümann (1989) found with LES. 2) There is a clear demarcation in potential temperature between the boundary layer and the inversion layer, and we take comfort that the line where $\partial \theta^* / \partial z^* = 0$ is in close proximity to $z_i^* = 0.7$. 3) The dimensional values of the potential temperature perturbations range from order $0.1\ K$ to $1.0\ K$; the lower value is in accordance with the results of Haack and Shirer (1992).

The wavenumber 3 and 4 patterns observed have only a minor effect on the vertical transport of thermal energy in the model (Figures 4.19 and 4.20). These convincing dimensionless heat flux profiles reveal small negative heat fluxes in the inversion layer, as is typically observed. Both figures also show maximum fluxes near the bottom of the domain, which is to be expected when there is heating from below. The magnitudes of the heat fluxes are of order $10^{-1} Kms^{-1}$ for Case 1, and order $10^{-2}\ Kms^{-1}$ for Case 2; the smaller values obtained in Case 2 are consistent with the findings of Laufersweiler and Shirer (1995), who also studied a quasi-two-dimensional case. The Case 2 heat flux profile (Figure 4.20) is especially encouraging, for it decreases nearly linearly from a relatively large positive value at $z^* = 0.15$ to a relatively small negative value at z_i^*; then above z_i^*, it increases in value towards zero, showing the entrainment (between $z^* = 0.6$ and $z^* = 0.7$)
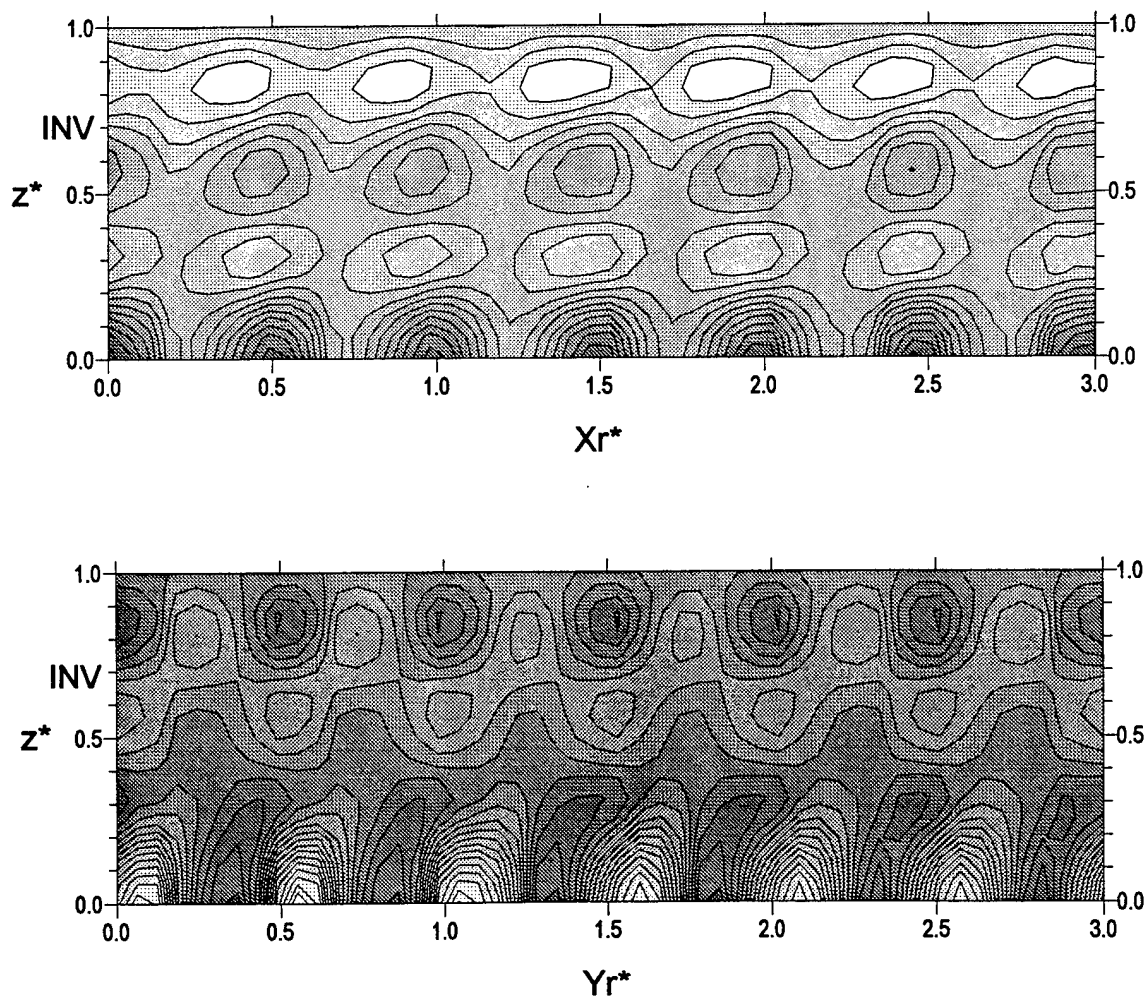
POTENTIALTEMPERATURE
CROSS SECTIONS
(CASE 1)

Figure 4.17. Cross sections of contoured potential temperature fields using rotated horizontal axes from Figure 4.7: (Top) θ^* is contoured along the Xr^* axis, and (Bottom) θ^* is contoured along the Yr^* axis. Shaded regions represent negative values while lighter regions represent positive values. The contour interval is consistent in the top and bottom frames, as well as with Figure 4.18.
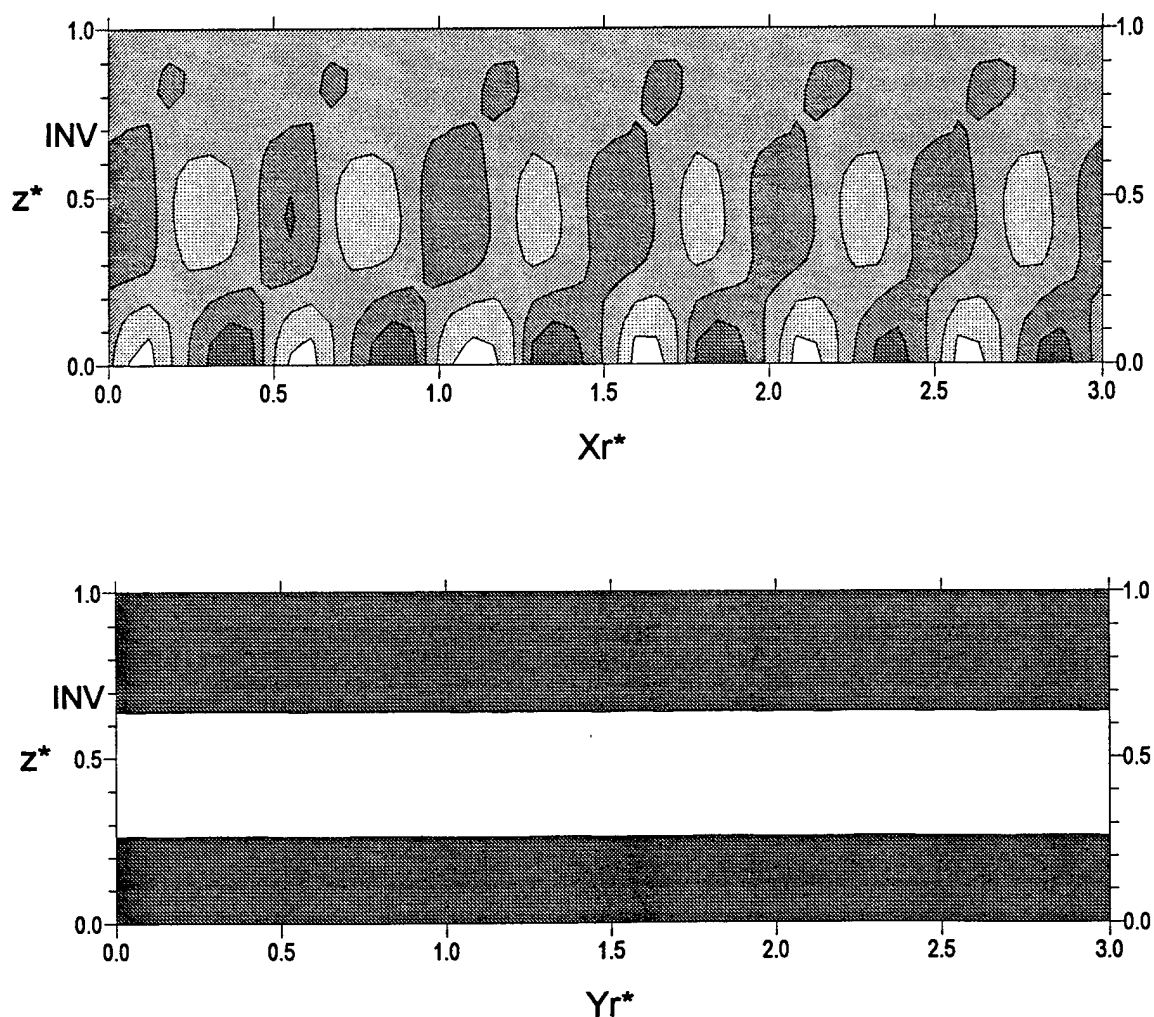
POTENTIALTEMPERATURE
CROSS SECTIONS
(CASE 2)

Figure 4.18. Cross sections of contoured potential temperature fields using rotated horizontal axes from Figure 4.9: (Top) θ^* is contoured along the Xr^* axis, and (Bottom) θ^* is contoured along the Yr^* axis. Shaded regions represent negative values while lighter regions represent positive values. The contour interval is consistent in the top and bottom frames, as well as with Figure 4.17.
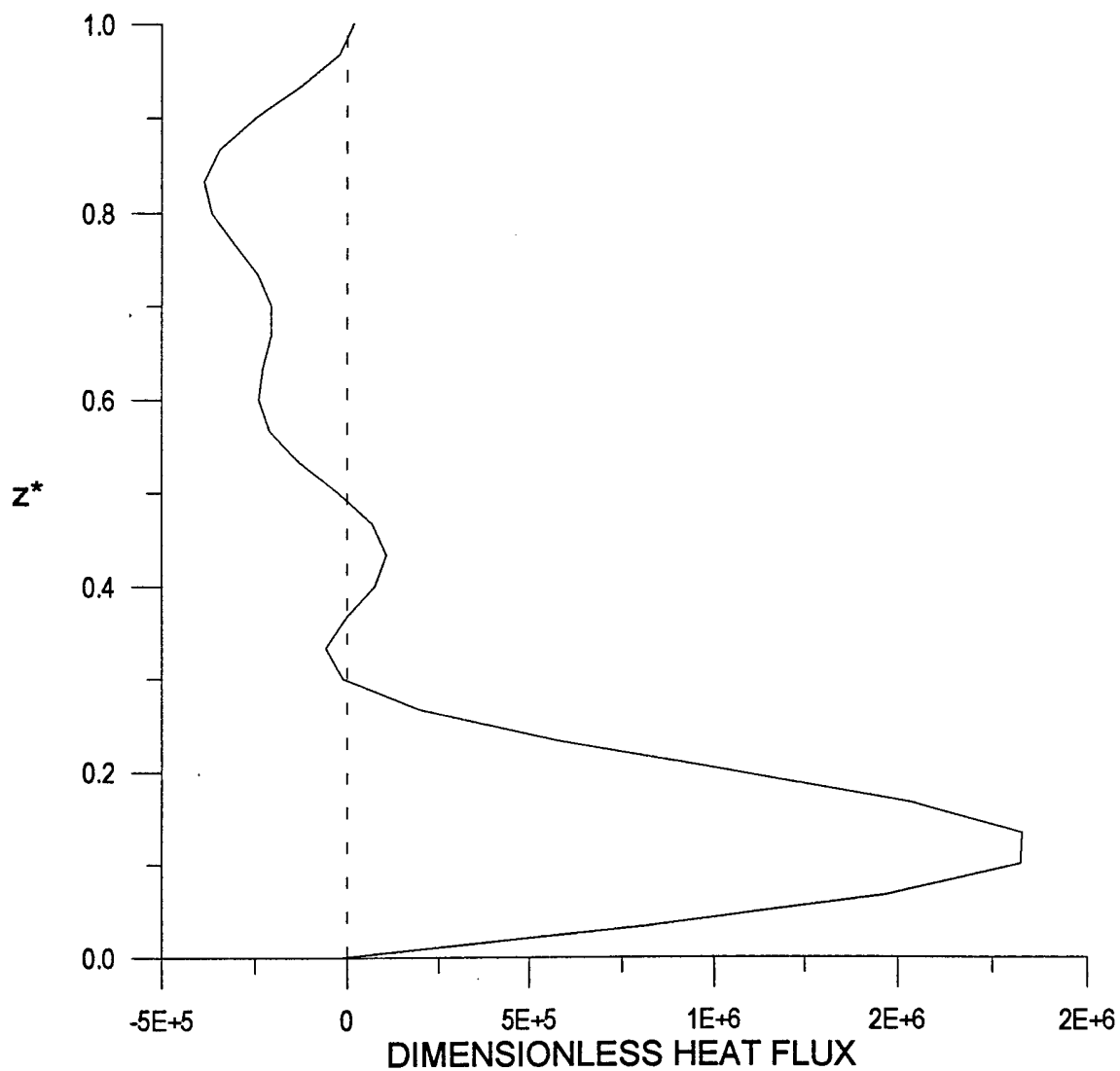
DIMENSIONLESS HEAT FLUX
(CASE 1)

Figure 4.19. Profile of the (layer-averaged) dimensionless heat flux for Case 1.
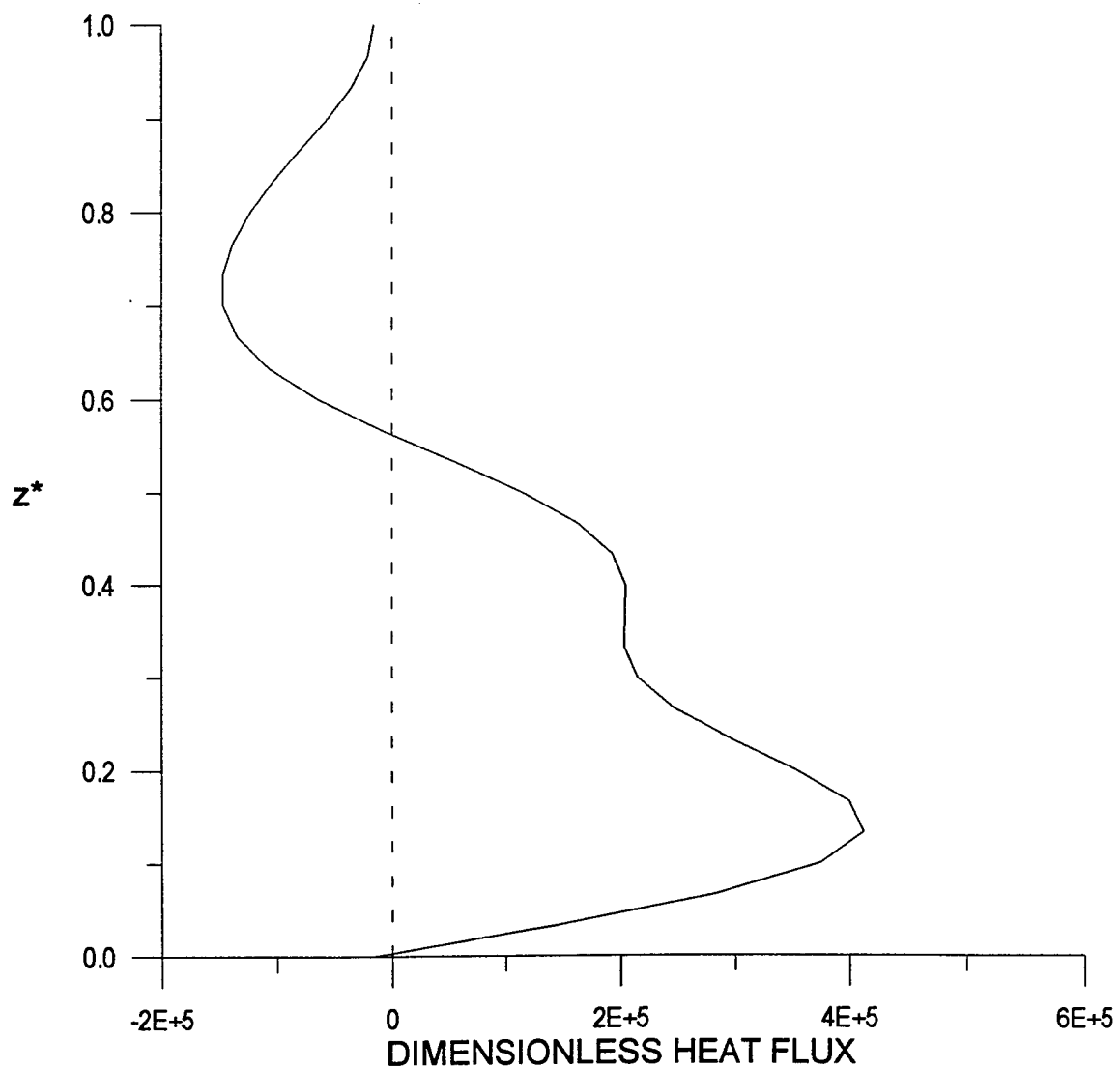
DIMENSIONLESS HEAT FLUX
(CASE 2)

Figure 4.20. Profile of the (layer-averaged) dimensionless heat flux for Case 2.

of warm inversion layer air into the boundary layer. At the lower boundary, however, the fluxes return to near zero values, which is not representative of a cool MABL over a warm ocean when the proper subgrid components are included. The heat flux reverts to zero as a consequence of the imposed boundary condition (2.36), but is acceptable for the BLCE scale (e.g., Brümmer 1985; Becker 1987; Chlond 1987).

The vertical transport of horizontal momentum (i.e., the mean momentum flux) is depicted in Figure 4.21 for Case 1 and Figure 4.22 for Case 2. Though lacking the detail given by calculating the momentum in the separate x^*- and y^*-components, these mean momentum profiles, which are calculated using standard flux equations (Stull 1988), are good indicators of the overall momentum transport by the model solutions. From Figure 4.22, we observe that the maximum flux of momentum occurs near $z^* = 0.35$ for Case 2. This is reassuring, for it is relatively consistent with our findings for the maximum vertical velocity, discussed earlier; we are also pleased that the flux values in the inversion are negligible. Case 1, which is shown in Figure 4.21, shows a local maximum at $z^* = 0.3$ but a much greater maximum in the inversion layer. While this correlates well with the Case 1 vertical velocity profile in Figure 4.15, as we expect, the presence of a momentum flux maximum in the inversion is somewhat disconcerting and worthy of further study.

The secondary circulations determined by the model alter the background mean wind profile through horizontally-independent modifications, which come only from the ψ_{0j} and η_{0j} components (Haack and Shirer 1992). In Figure 4.23 (Case 1) and Figure 4.24 (Case 2), we plot the background wind speed $|V(z)|$ and the modified plus background wind speed $|V(z) + v_{mod}(z)|$ on the same graph. This latter wind value at ($z^* = h_{LB}$), known also as the post roll/cell wind, is what would be diagnosed from a SAR image. For both cases, we clearly show that the BLCE circulations are redistributing the shear in the boundary layer, as was noted by Haack and Shirer (1992). We also note that the magnitude of the change in wind speed is in line with the findings of Haack and Shirer

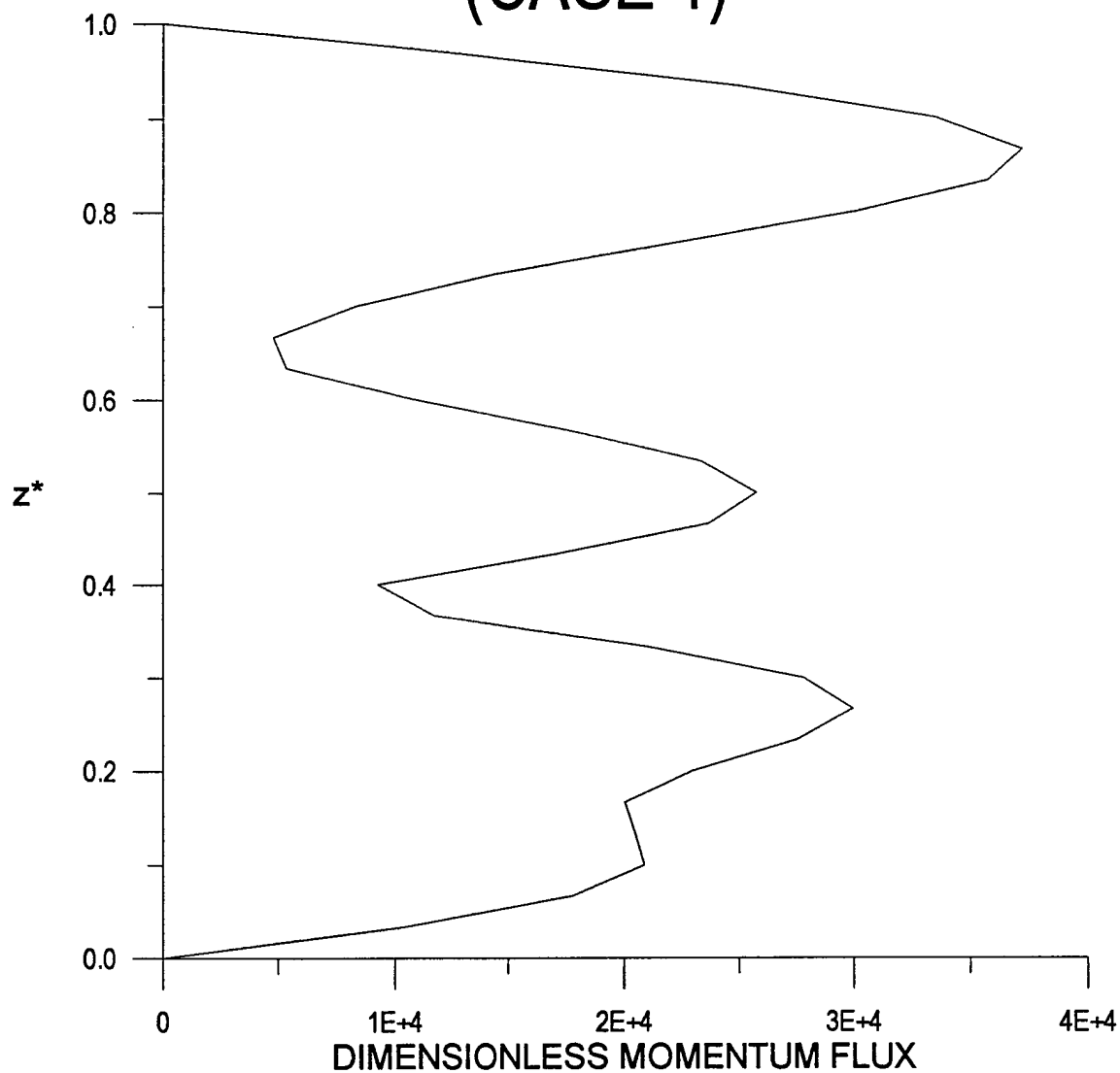# MEAN DIMENSIONLESS MOMENTUM FLUX (CASE 1)

Figure 4.21. Profile of (layer-averaged) dimensionless momentum flux for Case 1.
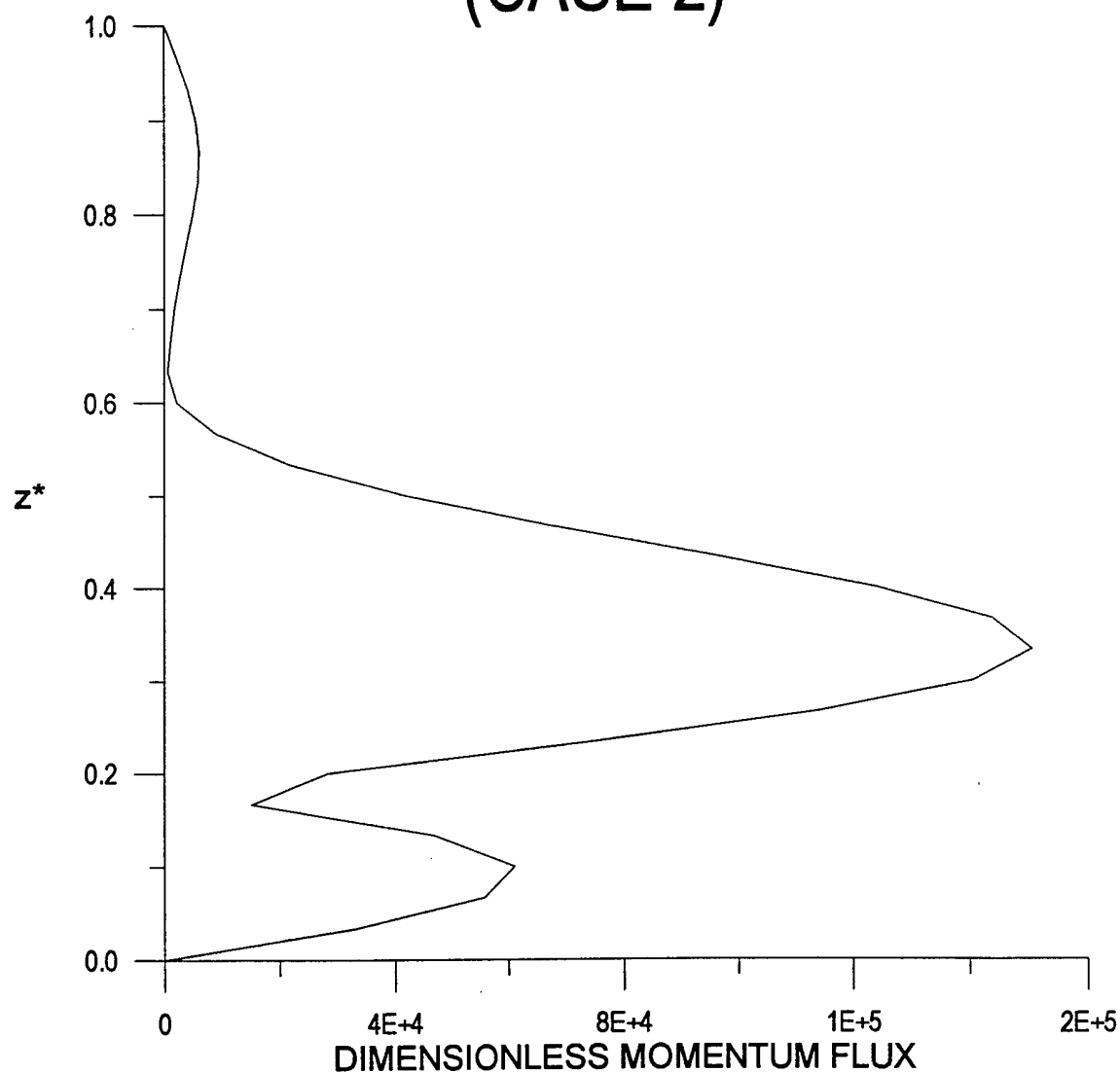
MEAN DIMENSIONLESS MOMENTUM FLUX (CASE 2)

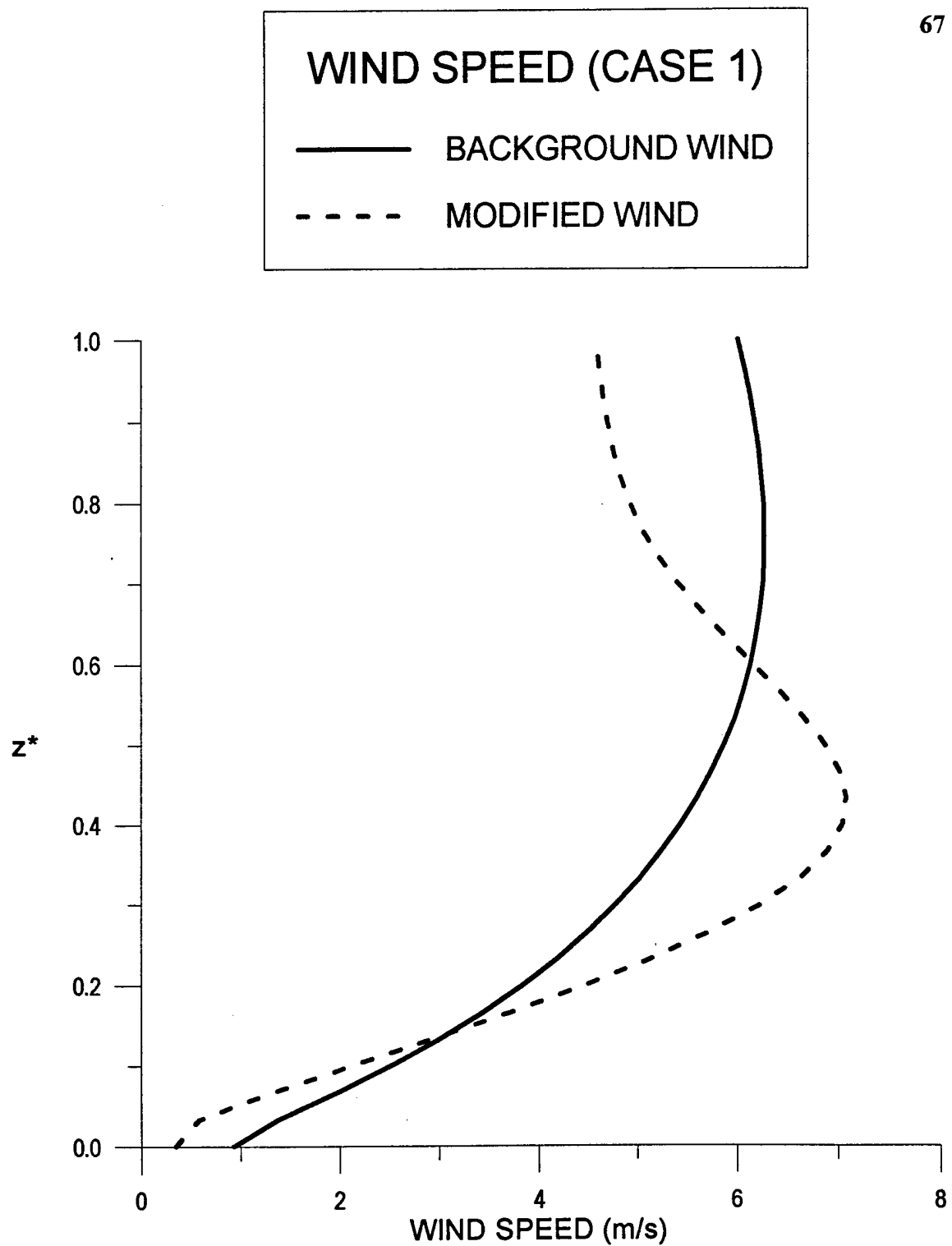Figure 4.22. Profile of (layer-averaged) dimensionless momentum flux for Case 2.

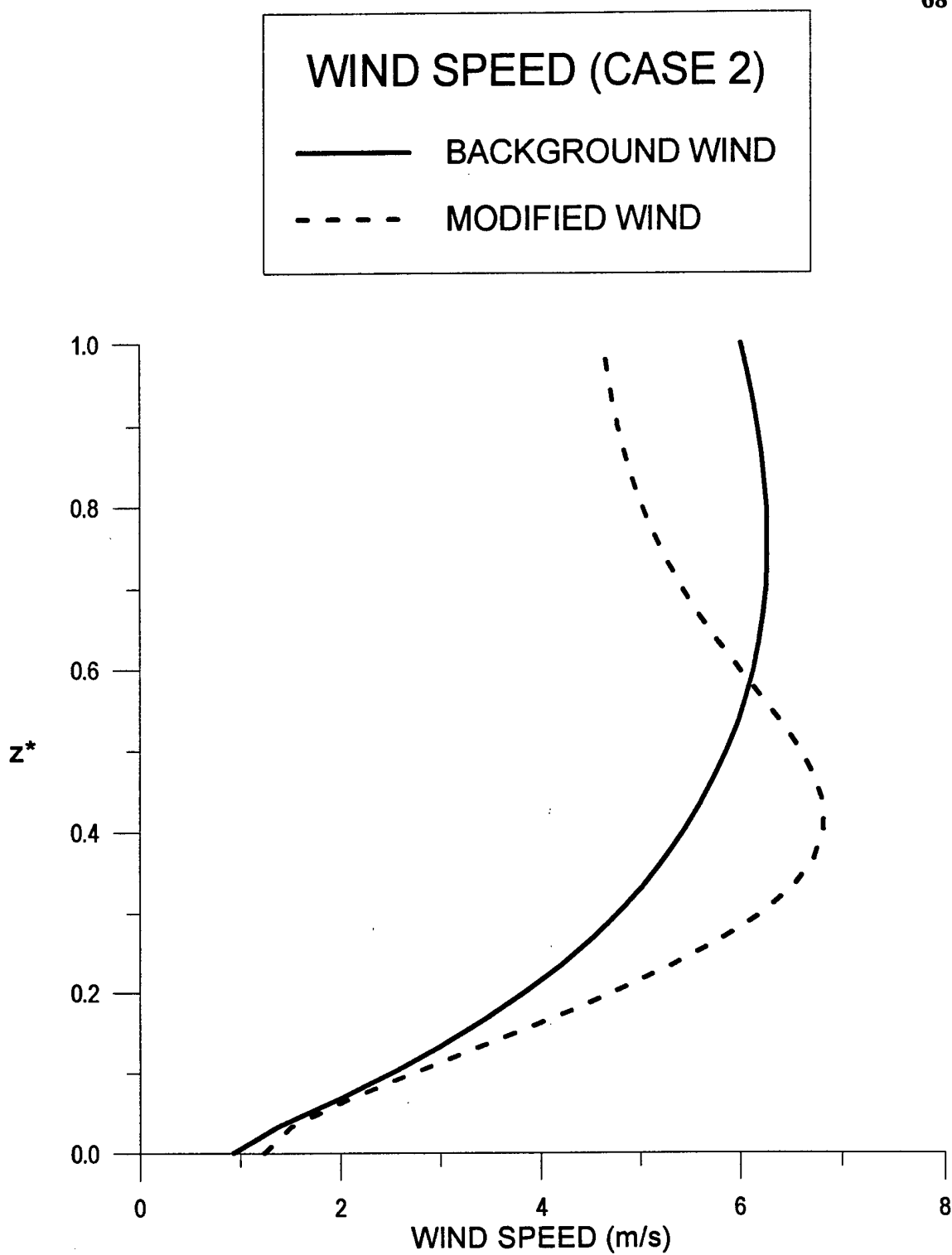Figure 4.23. Profile of background and modified (post-cell) wind speeds for Case 1.

Figure 4.24. Profile of background and modified (post-cell) wind speeds for Case 2.

(1992), and is sufficient to alter the linear analysis significantly. The modified wind speed profiles are quite similar for Cases 1 and 2, although the wind speed decreases more rapidly near the surface for Case 1, indicating slightly greater shear in the lowest portions of the MABL. According to the Woodcock (1975) diagram in Figure 4.1, we would expect regimes with stronger winds at 10 m (h_{LB}) to have a higher likelihood of becoming quasi-two-dimensional than regimes with weaker 10 m winds. This is consistent with our case study result because the modified wind speed at h_{LB} for Case 1 is approximately 0.4 m/s, while the speed at h_{LB} for Case 2 is 1.3 m/s. Though not a large absolute difference, the *relative* difference is not insignificant. We therefore postulate that Case 1 evolved into a three-dimensional solution consistent with the reduction in the wind speed at the lower boundary, while Case 2 remained a quasi-two-dimensional solution consistent with an increase in the wind speed at the lower boundary.

We further propose that the Woodcock (1975) diagram be reformulated as a statistical probability graph rather than an absolute predictor of regime type. We could do this by adding contours of constant probability to the chart to determine the odds of obtaining rolls or cells based upon the input parameter values (i.e., location on the diagram); such contours could be resolved experimentally based upon the relative number of runs that give quasi-two- or three-dimensional solutions. For example, the demarcation line between rolls and cells on Figure 4.1 would most likely represent the 50 percent probability line of obtaining one or the other regime type. Our early model runs also support a probabilistic approach to interpretation of the diagram (e.g., Table 4.4 for Case 1). In Figures 4.23 and 4.24, we observe that shear is minimal in the inversion layer, consistent with observations. Additionally, the modified wind speed profiles for each case contain two points of inflection, whereas the background wind speed profile contained none. We stated previously that an inflection point in the wind speed profile is a necessary condition for cells to align normal to the direction of the mean wind (Brown 1980), as we found for Case 1; however, it is not a sufficient condition because our Case 2 rolls aligned

70

nearly parallel to the direction of the mean wind despite the presence of inflection points in the modified wind profile.

The wind direction profiles, though not shown here, indicate negligible turning shear for Case 1 and moderate turning shear for Case 2. Essentially then, we classify Case 1 as a pure speed shear case, while we classify Case 2 as a speed and turning shear case. Case 1, whose cellular structure is aligned nearly normal to the mean wind, is fully consistent with Brown (1980); while Case 2, whose rolls are aligned 14^0 to the right of the background wind, is predicted to be 40^0 to the left of the mean wind. However, Brown (1980) notes that in cases with both speed and turning shear "rows may occur at various angles, often depending on the layer stratification, such that positive buoyancy acts to align the rows with the mean velocity." We are encouraged by these consistencies.

4.3. Case Study Conclusions

The results obtained in this study of the Sonde 1 case from Hi-Res 2 clearly show that the model is capable of capturing the spatial organization of roll and cell circulations in the MABL. The addition of an inversion layer appears to more realistically cap the secondary circulations (Laufersweiler and Shirer 1995) than did the rigid lid used in earlier runs and in other studies (e.g., Lambert 1995). In the presence of a quasi-equilibrated solution and weak to moderate forcing, we can now reasonably expect the inversion to consistently cap boundary layer secondary circulations. We are also pleased that the vertical profiles of heat and momentum fluxes respond well to the addition of an inversion layer, especially matching the results of Laufersweiler and Shirer (1995) for Case 2. The appearance of narrow updrafts and broad downdrafts in the Case 2 vertical velocity cross section is another encouraging aspect of our findings. Most notable, however, is the ability of the model to reproduce realistic stress patterns at the lower boundary and to select appropriate orientation angles relative to the mean background wind. In developing their

algorithm to extract wind data from SAR imagery, Wackerman *et al.* (1996) made the assumption that stress patterns are inherently aligned with the direction of the mean background wind "to within a 180^0 ambiguity." In most cases during our study--about 95 percent of the time--we found this to be true and therefore concur that they have made a valid assumption. However, we must always remember that it is *possible* for rolls and cells to align normal to the direction of the mean wind, especially in the presence of an inflection point in the wind profile; our Case 1 results lucidly convey this result.

Overall, the model performed well in replicating the atmospheric conditions of Hi-Res 2. During the course of our research, however, we noted several areas that should be addressed in the near future:

1) After implementing the inversion subroutine and a numerically accurate temporal finite differencing scheme, we did not find attainment of a fully equilibrated model solution to be possible within a reasonable amount of time. The addition of a surface layer, nonlinear diffusion and a scale factor s_f have helped tremendously, but we feel that further numerical techniques are required to increase the speed of integration, without compromising the accuracy. Another option would be to find better seed initial conditions--using the last vector y from Case 2 (at 150,000 s) would be a good starting point for all future case studies. Should these proposals not resolve the problem, we recommend that more vertical wavenumbers be added to the model to improve the resolution given by the spectral truncation. The addition of more horizontal wavenumbers, which would allow the representation of cell broadening (Chang and Shirer 1984), is warranted as well.

2) The subgrid parameterization of fluxes should be addressed so that qualitatively correct heat and momentum flux calculations can be obtained down to the lower boundary height h_{LB}. This might be accomplished by inserting subgrid heat flux terms (produced

only by the horizontally-independent modification coefficients θ_{0j}) into the roll potential temperature NDS equations for $\dot{\theta}_{ij}$ (2.39). Such a parameterization would be an application of the eddy form

$$\frac{\partial \theta'}{\partial t} \approx -\frac{\partial}{\partial z} \overline{(w''\theta'')} \approx \kappa \frac{\partial^2 \theta_m}{\partial z^2}, \tag{4.6}$$

where the double primes denote sub-model values where the number of wavenumbers exceeds four and θ_m is the height-only-dependent portion of the θ^* expansion in (2.39).

3) Study the linear portion of the model more fully to determine the sensitivity of the preferred a_x and a_y values to the wind profile, inversion strength and other parameters.

4) Experiment further with the scale factor s_f, nonlinear dissipation rate d and the surface layer depth z_{SL} to better understand the effects they (individually and collectively) have on the model solutions. An emphasis should be placed on the physical significance of these numerical adjustments.

5) Create an algorithm (to improve Woodcock's [1975] diagram) to assist in predicting the expected structural type of a given regime. We need to define how the winds at the top of the domain or how the inversion strength should best be incorporated to make improved planform predictions, as well as assess the plausibility of converting the diagram to one of probability type, on which lines of equal probability of observing a planform dimension are given. For instance, this would help us determine whether or not our quasi-two-dimensional Case 2 is likely to occur in the MABL with the given parameter values, even though it lies in the cellular regime.

6) Develop a three-dimensional visualization algorithm that is incorporated into all future model development.

7) Study further the presence of vertical velocity and momentum flux maxima in the inversion layer for Case 1.

8) Conduct case studies using Hi-Res 2 Sonde 2 data, listed in Table 4.1, as well as other cases from subsequent field projects.

Significant alterations have been made to the model during the course of this study, and we are pleased that model solutions have improved greatly as a result. With the implementation of the recommendations noted above, the model should become a reliable tool to help ascertain the impact that BLCE have on stress at the sea surface by defining typical wind profiles and profile modifications, and by giving structural types of stress patterns.

REFERENCES

Alpers, W. and B. Brümmer, 1994: Atmospheric boundary layer rolls observed by the synthetic aperture radar: A review. *Rev. Geophys. Space Phys.*, **99**, 12613-12621.

Becker, P., 1987: Three-dimensional investigations of roll vortices: A Case study. *Contrib. Atmos. Phys.*, **60**, 170-179.

Brown, R. A., 1980: Longitudinal instabilities and secondary flows in the planetary boundary layer: A review. *Rev. Geophys. Space Phys.*, **18**, 683-697.

Brümmer, B., 1985: Structure, dynamics and energetics of boundary layer rolls from Kon Tur aircraft observations. *Contrib. Atmos. Phys.*, **58**, 237-254.

Chang, H. R. and H. N. Shirer, 1984: Transitions in shallow convection: An explanation for lateral cell expansion. *J. Atmos. Sci.*, **41**, 2334-2346.

Chlond, A., 1987: A numerical study of horizontal roll vortices in neutral and unstable atmospheric boundary layers. *Contrib. Atmos. Phys.*, **60**, 144-169.

Deardorff, J. W., 1976: Discussion of "thermals over the sea and gull flight behavior". *Bound. Lay. Meteo.*, **10**, 241-246.

Etling, D. and R. A. Brown, 1993: Roll vortices in the planetary boundary layer: A review. *Bound. Lay. Meteo.*, **65**, 215-248.

Faller, A. J., 1965: Large eddies in the atmospheric boundary layer and their possible role in the formation of cloud rows. *J. Atmos. Sci.*, **22**, 176-184.

Gerling, T. W., 1986: Structure of the surface wind field from the Seasat SAR. *J. Geophys. Res.*, **91**, 2308-2320.

Haack, T. and H. N. Shirer, 1992: Mixed convective-dynamic roll vortices and their effects on initial wind and temperature profiles. *J. Atmos. Sci.*, **49**, 1181-1201.

Higgins, R. W., 1987: From the equations of motion to spectral models. *Nonlinear Hydrodynamic Modeling: A Mathematical Introduction. Lecture Notes in Physics*, **271**, H. N. Shirer, Ed., Springer-Verlag, 47-69.

Kundu, P. K., 1990: *Fluid Mechanics*. Academic Press, San Diego, 638 pp.

Lambert, B. A. Jr., 1995: Sea surface stress variability in the boundary layer. MS Thesis, The Pennsylvania State University, 77 pp.

Laufersweiler, M. J., 1987: The expected branching solution: Preferred wavelengths. *Nonlinear Hydrodynamic Modeling: A Mathematical Introduction. Lecture Notes in Physics*, **271**, H. N. Shirer, Ed., Springer-Verlag, 131-163.

Laufersweiler, M. J. and H. N. Shirer, 1995: A theoretical model of multiregime convection in a stratocumulus-topped boundary layer. *Bound. Lay. Meteo.*, **73**, 373-409.

Lenschow, D. H., J. C. Wyngaard, and W. T. Pennell, 1980: Mean field and second moment budgets in a baroclinic convective boundary layer. *J. Atmos. Sci.*, **37**, 1313-1326.

Lilly, D. K., 1966: On the instability of Ekman boundary flow. *J. Atmos. Sci.*, **23**, 481-494.

Lorenz, E. N., 1993: *The Essence of Chaos.* University of Washington Press, Seattle, 227 pp.

Mourad, P. D., 1996: Inferring multiscale structure in atmospheric turbulence using satellite-based synthetic aperture radar imagery. *J. Geophys. Res.*, **101-C8**, 18433-18449

Press, W. H., W. T. Vetterling, S. A. Teukolsky, B. P. Flannery, 1992: *Numerical Recipes in FORTRAN; The Art of Scientific Computing, 2nd Ed.* Cambridge University Press, New York, 963 pp.

Pyle, R. J., 1987: Typical branching forms: Periodic solutions. *Nonlinear Hydrodynamic Modeling: A Mathematical Introduction. Lecture Notes in Physics*, **271**, H. N. Shirer, Ed., Springer-Verlag, 264-291.

Schmidt, H. and U. Schümann, 1989: Coherent structure of the convective boundary layer derived from large-eddy simulations. *J. Fluid Mech.*, **200**, 511-562.

Shirer, H. N., 1986: On cloud street development in three dimensions: Parallel and Rayleigh instabilities. *Contrib. Atmos. Phys.*, **59**, 126-149.

Shirer, H. N., Ed., 1987: *Nonlinear Hydrodynamic Modeling: A Mathematical Introduction. Lecture Notes in Physics*, **271**, Springer-Verlag, 546 pp.

Shirer, H. N., B. A. Lambert, Jr., L. V. Zuccarello, R. Wells, T. D. Sikora, 1996: Brightness variability on synthetic aperture radar imagery of the sea surface caused by kilometer-scale atmospheric convective eddies. *Proc. Oceans '96 MTS/IEEE Conf.*, **3**, 1396-1399.

Shirer, H. N., D. J. Beberwyk, B. A. Lambert, L. V. Zuccarello, R. Wells, T. D. Sikora, 1997: Kilometer-scale patterns on synthetic aperture radar imagery of the sea surface caused by marine atmospheric boundary layer convective eddies. *Proc. 12th Bound. Lay. and Turb. Conf.*, American Meteorological Society, in press.

Sikora, T. D., G. S. Young, R. C. Beal, and J. B. Edson, 1995: Use of spaceborne synthetic aperture radar imagery of the sea surface in detecting the presence and structure of the convective marine atmospheric boundary layer. *Mon. Wea. Rev.*, **123**, 3623-3632.

Stensrud, D. J. and H. N. Shirer, 1988: Development of boundary layer rolls from dynamic instabilities. *J. Atmos. Sci.*, **45**, 1007-1019.

Stull, R. B., 1988: *An Introduction to Boundary Layer Meteorology*. Kluwer Academic Publishers, Boston, 666 pp.

Thompson, T. W., W. T. Liu, D. E. Weissman, 1983: Synthetic aperture radar observation of ocean roughness from rolls in an unstable marine boundary layer. *Geophys. Res. Lett.*, **10**, 1172-1175.

Vesecky, J. F. and R. H. Stewart, 1982: The observation of ocean surface phenomena using imagery from the SEASAT synthetic aperture radar: An assessment. *J. Geophys. Res.*, **87**, 3397-3430.

Wackerman, C. C., C. L. Rufenbach, R. A. Shuchman, J. A. Johannessen and K. L. Davidson, 1996: Wind vector retrieval using ERS-1 synthetic aperture radar imagery. *IEEE Trans. Geosci. Rem. Sens.*, **34**, 1343-1352.

Woodcock, A. H., 1940: Convection in the atmospheric boundary layer. *J. Marine Res.*, **3**, 248-253.

Woodcock, A. H., 1975: Thermals over the sea and gull flight behavior. *Bound. Lay. Meteo.*, **9**, 63-68.

Zuccarello, L. V., 1994: Modeling sea–surface stress variability caused by kilometer–scale marine atmospheric boundary layer circulations. MS Thesis, The Pennsylvania State University, 64 pp.